

LIBRARY Michigan State University

This is to certify that the

dissertation entitled

CHARACTERISTICS OF CHARM PARTICLES PRODUCED BY 800 GEV P-P COLLISIONS

presented by

Ai Gia Nguyen

has been accepted towards fulfillment of the requirements for

Doctor of Philosophy degree in Physics

Major professor

Date April 25, 1988



RETURNING MATERIALS:
Place in book drop to remove this checkout from your record. FINES will be charged if book is returned after the date stamped below.

CHARACTERISTICS OF CHARM PARTICLES PRODUCED BY 800 GEV P-P COLLISIONS

Вy

Ai Gia Nguyen

A DISSERTATION

Submitted to
Michigan State University
in partial fullfillment of the requirements
for the degree of

DOCTOR OF PHILOSOPHY

Department of Physics and Astronomy

ABSTRACT

CHARACTERISTICS OF CHARM PARTICLES PRODUCED BY 800 GEV P-P COLLISIONS

By

Ai Gia Nguyen

This thesis presents the results of Fermilab experiment E743, a study of the production characteristics of the D mesons in 800 GeV proton-proton collisions ($\sqrt{s}=39$ GeV), utilizing a high resolution, rapid cycling bubble chamber for vertex detection, and a multiparticle spectrometer for the momentum determination of charged particles. A relatively unbiased measurement of the D meson cross section is accomplished by direct observation of the decay vertices in the bubble chamber, $\sigma(D/\overline{D})=59^{+22}_{-15}\mu$ b. Also measured are the longitudinal and transverse momentum distributions of observed D meson decays. The differential production cross sections are described well by the form

$$\frac{1}{\sigma} \frac{d^2 \sigma}{dx_F dp_T^2} = (n+1)(\frac{b}{2})(1-|x_F|)^n e^{-bp_T^2}$$

with n = $11.0^{+4.6}_{-3.6}$ and b = $0.66^{+0.23}_{-0.20}$ (GeV/c)⁻². For $|x_F| > 0.3$ we observe no events, which corresponds to an upper limit of 10 μ b at a 95 % confidence level.

When compared with measurements made at lower energies the results of this study point to a D meson cross section which is slowly rising with center of mass energy. These results are in sharp contrast with the results from a number of experiments performed at the CERN Intersecting Storage Rings (ISR) ($\sqrt{s} = 53\text{-}62 \text{ GeV}$) which indicated a dramatic rise in the charm particle cross sections with increasing energy. These large cross sections were observed in experiments which were sensitive to production at large x_F values (typically $x_F > 0.3$). Unusual mechanisms for charm production invoked to explain these large cross sections do not appear to be necessary below $\sqrt{s} = 39 \text{ GeV}$. Also, our longitudinal momentum distribution of D mesons shows no evidence of production at large x_F . A more generally accepted model for charm hadronic production, the Fusion model, can reproduce most aspects of our data.

ACKNOWLEDGMENTS

This thesis was written with the support and guidance of Professor Carl Bromberg of Michigan State University. I would like to thank him, as well as Drs. Roger Dixon, Howard Fenker, Ian Leedom, John Marraffino, and Steve Reucroft for invaluable comments and discussions. I would also like to thank our other collaborators and the dedicated staff of the Fermilab Film Analysis Facility. The following fourteen institutions participated in the LEBC-MPS collaboration: Aachen, Berlin-Zeuthen, Brussels, CERN, Duke, Fermilab, Kansas, Michigan, Michigan State, Mons, Notre Dame, Tata (Bombay), Vanderbilt, and Vienna. I thank also the Sage Foundation for providing me with a grant towards publication costs for this thesis.

I thank Trang for her patience and forbearance, and my parents for their constant moral and occasional financial support.

TABLE OF CONTENTS

List of Tables	vii
List of Figures	viii
1 Introduction	1
2 Theoretical and Experimental Perspectives	3
2.1 Properties of the charm quark	3
2.2 Parallel attempts to measure charm hadronic cross sections	8
2.3 Attempts to measure charm differential cross sections in x_F and p_T^2	15
2.4 Two mechanisms for hadronic production of charm	15
2.5 Summary of the goals and results of E743	21
3 Experimental Apparatus	26
3.1 The beam and beam optics	26
3.2 LEBC, the hydrogen target and vertex detector	30
3.3 The FMPS spectrometer	34
3.4 The triggers and data acquisition system	40
4 Data Reduction	44
4.1 Film analysis	44
4.1.1 Scanning	45
4.1.2 Measuring	50
4.2 Event reconstruction	51
4.2.1 Spectrometer tracking	51

4.2	.2 Hybridisation and kinematic fitting	52
4.2	.3 Graphical techniques	55
5	Normalization and Multiplicity Distribution	59
5.1	Scanning of the data sample taken with an unbiased trigger	59
5.2	Determination of the multiplicity distribution	61
5.3	Determination of the interaction trigger bias	68
6	Determination of the Charm Inclusive Cross Section	71
6.1	Normalization and systematic uncertainties	71
6.2	Cross section results	74
7	D Meson Differential Cross Sections	76
7.1	Observations based on film measurement	77
7.2	Observations based on spectrometer information	78
7.3	Differential cross section results	86
8	Comparison of Results with the Fusion Model and Other Mechanisms	- 90
8.1	The experimentally observed energy dependence of the charm cross sections	. 90
8.2	Predictions by the Fusion model and by other mechanisms	93
9	Conclusions	101

Appendices

A	The Impact Parameter of Decay Tracks	104
В	Simulating Charm Decays	106
C	The 0°C Calculation	110

LIST OF TABLES

2.1	Predicted pseudoscalar charm mesons	6
2.2	The single charm baryons	7
2.3	A partial list of charm cross section measurements	12
2.4	A partial list of measurements for the production parameters n and b	16
3.1	Important LEBC parameters	36
4.1	Spectrometer acceptance as a function of x_F and topology (V2, C3, V4), requiring all charged decay tracks to be reconstructed	56
4.2	Spectrometer acceptance as a function of x_F and topology (V2, C3, V4), requiring at least two charged decay tracks to be reconstructed	57
5.1	Scanning efficiency for the multiplicity sample	60
5.2	Observed topological cross sections	63
5.3	Lowest moments of the observed inclusive multiplicity distribution	65
6.1	The D meson sample and effects of the geometrical cuts	74
7.1	Reconstructed D meson decays	85
C.1	Corrections for the slow 0°C solution	112

LIST OF FIGURES

2.1	Charm cross section vs. center of mass energy	13
2.2	Charm partial cross section ($ x_F > 0.3$) vs. center of mass energy	14
2.3	First order diagrams for the (a)Fusion and (b)Excitation processes	18
3.1	Optics of the MT beam line	27
3.2	Site map showing the location of the MT beam line	28
3.3	A photograph of our LExan Bubble Chamber	31
3.4	Beam's eye view of the chamber assembly	32
3.5	Vacuum tank and camera set up for LEBC	33
3.6	The optical system of LEBC.	35
3.7	Elevation view of the Fermilab Multiparticle Spectrometer in the E743 configuration	38
3.8	The E743 trigger system	41
3.9	Timing of our interaction trigger	42
4.1	An illustration of (a)important decay parameters and of the charm topologies (b)C3 and (c)V4	46
4.2	Photograph of a charm event	49
5.1	The multiplicity distribution	64
5.2	The energy dependence of the mean charge multiplicity	66
5.3	Energy dependence of the (normalized) higher multiplicity moments	67
5.4	Efficiency of our interaction trigger	70
7.1	The longitudinal decay length distribution	79
7.2	The transverse decay length distribution	80

7.3	Maximum likelihood fit of the longitudinal decay length distribution	81
7.4	Maximum likelihood fit of the transverse decay length distribution	82
7.5	The Feynman x distribution $\frac{dN}{ds_p}$	87
7.6	The invariant distribution E_{dop}^{dN}	88
7.7	The transverse momentum distribution $\frac{dN}{dp_T^2}$	89
8.1	Fusion model predictions of the integrated charm hadronic production cross section	95
8.2	Fusion model predictions of the differential charm hadronic production cross section $\frac{dN}{da_P}$	96
8.3	Fusion model predictions of the differential charm hadronic production cross section $\frac{dN}{dp_T^2}$	97
B.1	Simulated $D^+ \to K^-\pi^+\pi^+$ decays, part 1	108
B.2	Simulated $D^+ \to K^-\pi^+\pi^+$ decays, part 2	109

Chapter 1

INTRODUCTION

This thesis presents the results of Fermilab experiment E743, a study of 800 GeV proton-proton collisions (center of mass energy $\sqrt{s} = 39$ GeV), utilizing a high resolution, rapid cycling bubble chamber for vertex detection, and a multiparticle spectrometer for the momentum determination of charged particles. The study emphasizes the measurement of the production characteristics of the meson states containing a charm quark, specifically the D mesons. The most important measurement made is the D meson inclusive cross section. A relatively unbiased measurement of the D meson cross section is accomplished by direct observation of the decay vertices in the bubble chamber. Also measured are the longitudinal and transverse momentum distributions of observed decays, as well as the multiplicity of charged particles produced in both charm and non-charm associated events.

When compared with measurements made at lower energies the results of this study point to a D meson cross section which is slowly rising with center of mass energy. These results are in sharp contrast with the results from a number of exper-

iments performed at the CERN Intersecting Storage Rings (ISR) which indicated a dramatic rise in the charm particle cross sections with increasing energy. These large cross sections were observed in experiments which were sensitive only to production at large values of x_F ($x_F \equiv \frac{p_{\parallel}}{p_{\parallel,max}}$, where p_{\parallel} is the longitudinal momentum in the center of mass frame, and $p_{\parallel,max}$ is its maximum value). We show that unusual mechanisms for charm production, invoked at that time to explain large cross sections, are unnecessary to explain the energy dependence of charm production below $\sqrt{s} = 39$ GeV. We also show that the longitudinal momentum distribution of D mesons observed in our study is steeply peaked at $x_F = 0$ and shows no evidence for production at large x_F .

We have also compared our data to a more generally accepted model for hadronic production. This model, which makes use of the fundamental Quantum Chromodynamic (QCD) scattering amplitudes between quarks and gluons, and a phenomenological picture of the structure of the proton as well as the hadronization of a quark, can reproduce most aspects of our data.

This thesis begins with a discussion of the historical background and issues in charm production physics, the motivation for the configuration of our experimental apparatus, and is followed by the presentation of the experimental results and conclusions.

Chapter 2

THEORETICAL AND EXPERIMENTAL PERSPECTIVES

2.1 Properties of the charm quark

Before 1970, in the Cabibbo model¹ the up, down, and strange quarks are arranged in a doublet,

$$\left(egin{array}{c} u \ dcos heta_c+ssin heta_c \end{array}
ight),$$

expressing the fact that the down and strange quarks participating in the weak interaction are rotated by the Cabibbo angle θ_c . The weak neutral current is of the form

$$J^{\circ} \sim u\overline{u} + d\overline{d}\cos^2\theta_c + s\overline{s}\sin^2\theta_c + (s\overline{d} + \overline{s}d)\sin\theta_c\cos\theta_c$$

with a nonzero strangeness changing component (the last term), in conflict with experimental limits² established by measurements of decays of the neutral K meson

¹N. Cabibbo, Phys. Rev. Lett. <u>10</u> (1963) 531

²Particle Data Group, Revs. Mod. Phys. <u>52</u> (1980) 1

such as

$$\frac{\Gamma(K_L^o \to \mu^+ \mu^-)}{\Gamma(K_L^o \to all)} = (9.1 \pm 1.9) \times 10^{-9}.$$

In 1970, the charm quark was proposed by Glashow, Iliopoulos, and Maiani ³ as part of a model (the GIM model) to explain the lack of a strangeness changing neutral current in weak interactions. The charm quark was introduced in an additional doublet,

$$\left(egin{array}{c} c \ scos heta_c-dsin heta_c \end{array}
ight).$$

The weak neutral current gains a term

$$J^o \rightarrow J^o - (s\overline{d} + \overline{s}d)sin\theta_c cos\theta_c$$

and the strangeness changing component is cancelled.

At the time of the proposal of the GIM model, there was yet no experimental evidence for the charm quark. Indirect but compelling evidence was provided in 1974 by the discovery of the $J/\psi^{4,5}$, a massive (3.1 GeV/ c^2) spin one particle. The large mass and low spin of the J/ψ suggested that it was a low lying bound state of heavy quarks. Subsequently, several resonances were observed at higher masses, including the ψ' (3685) and ψ'' (3770). These resonances were interpreted as excited states of the $c\bar{c}$ system. The ψ'' in particular played an important role in spectroscopic studies of the D meson, the first observed quark system with nonzero charm quantum number

³S. L. Glashow, J. Iliopoulos, and L. Maiani, Phys. Rev. <u>D2</u> (1970) 1285

⁴J. J. Aubert et al., Phys. Rev. Lett. <u>33</u> (1974) 1404

⁵J. E. Augustin et al., Phys. Rev. Lett. <u>33</u> (1974) 1406

(open charm).

Direct evidence for the existence of the charm quark was obtained in 1976 by the observation, in e^+e^- annihilations, of narrow mass peaks in the $K^\pm\pi^\mp$, $K^\pm\pi^\mp\pi^\mp$, and $K^\pm\pi^\mp\pi^+\pi^-$ systems at 1.9 Gev/ $c^{26,7}$. Following the discovery of the ψ'' in 1977, large samples of D decays became available. The ψ'' is only 40 MeV above the D meson pair threshold and provides a copious and clean source of these particles.

The existence of four quarks implied an extension of the hadron spectrum. The SU(3) meson octet of pions, kaons, and η became an SU(4) fifteen-plet, and the SU(3) baryon octet of nucleons, Σ 's, and cascades became an SU(4) twenty-plet⁸. Table 1 lists the predicted pseudoscalar charm mesons and table 2 gives the single charm baryons.

Experimental evidence exists for a number of these low lying meson and baryon states. The TPS collaboration has reported a D_s signal in the $\phi\pi^+, \phi\pi^-, K^{*o}K^-$, and $\overline{K}^{*o}K^+$ channels in photon-nucleon collisions. The charm baryon Λ_c has been observed by experiments at the CERN ISR¹⁰. The WA42 collaboration has reported evidence for the A^+ baryon¹¹ in Σ^-Be collisions in the $\Lambda K^-\pi^+\pi^+$ channel. Excited

⁶G. Goldhaber et al., Phys. Rev. Lett. <u>37</u> (1976) 255

⁷I. Perussi et al., Phys. Rev. Lett. 37 (1976) 569

⁸M. K. Gaillard, B. W. Lee, and J. Rosner, Rev. Mod. Phys. 47 (1975) 277

⁹M. S. Witherell, Procs. of the Salt Lake City Meeting of the DPF (1987) 135

¹⁰D. DiBitonto, AIP Conference Proceedings No. 85 (1981) 26

¹¹S. F. Biagi et al., Phys. Lett. <u>150B</u> (1985) 230

Table 2.1: Predicted pseudoscalar charm mesons.

Name	Content	Isospin	Strangeness	Charm
D ⁺	$c\overline{d}$	1/2, 1/2	0	1
D°	$c\overline{u}$	1/2,-1/2	0	1
$D^+_{\bullet}(F^+)$	c s	0,0	1	1
$\overline{D}^{m{o}}$	<u></u> cu	1/2, 1/2	0	-1
D-	cd	1/2,-1/2	0	-1
$D_{ullet}^-(F^-)$	c̃ s	0,0	-1	-1
η_c	$c\overline{c}$	0,0	0	0

states of the D meson, the D^* , have been seen. The D^{*+} was observed as a clear peak in the $D^*\sigma^+$ system¹². Evidence for the other predicted charm states is statistically much weaker and not compelling.

A substantial body of spectroscopic information for the D mesons exists, from the Lead Glass Wall (LGW)¹³, MARK II¹⁴ and MARK III¹⁵ detectors at SLAC, and more recently from the Tagged Photon Spectrometer (TPS)¹⁶ at Fermilab. The masses, lifetimes, and branching ratios for Cabibbo favored decays of the charged and

¹²G. J. Feldman et al., Phys. Rev. Lett. 38 (1977) 1313

¹⁸I. Perussi et al., Phys. Rev. Lett. <u>39</u> (1977) 1301

¹⁴R. H. Schindler et al., SLAC-PUB-2507

¹⁵R. M. Baltrusaitis et al., Phys. Rev. Lett. <u>54</u> (1985) 1976

¹⁶M. S. Witherell, Procs. of the Salt Lake City Meeting of the DPF (1987) 135

Table 2.2: The single charm baryons; the S and A baryons have the same quark contents and are distinguished by their symmetry under simultaneous interchange of spin and label for the light quark pair.

Name	Content	Isospin	Strangeness	Charm
$C_1^{++}(\Sigma_c^{++})$	cuu	1, 1	0	1
$C_1^+(\Sigma_c^+)$	cud	1, 0	0	1
$C_1^o(\Sigma_c^o)$	cdd	1,-1	0	1
$C_o^+(\Lambda_c)$	cud	0,0	0	1
S ⁺	cus	1/2, 1/2	-1	1
S°	cds	1/2,-1/2	-1	1
A +	cus	1/2, 1/2	-1	1
A°	cds	1/2,-1/2	-1	1
T°	CSS	0,0	-2	1

neutral D mesons are relatively well known. Much less information is available for the decays of the D_s and Λ_c , although their masses and lifetimes are relatively well established.

2.2 Parallel attempts to measure charm hadronic cross sections

Charm is produced in hadronic collisions with cross sections near 10⁻³ of the total cross section, so that charm detection in hadronic processes is difficult. Apart from our measurements at 800 GeV, results are available at lower energies from fixed target experiments with 200 to 400 GeV/c hadron beams, and at higher energies from experiments at the CERN ISR.

There are three general approaches to the measurement of charm production in hadronic processes: inclusive lepton measurement, a mass peak search, or direct observation of charm decays. In the first approach, taken by several early experiments both at Fermilab and at CERN, the rate of prompt neutrinos or muons was used as an indirect measure of the charm production cross sections ¹⁷. Although models for charm production were needed to calculate the acceptance for the prompt leptons in the apparatus, copious production in hadronic collisions was ruled out.

Initial high statistics searches for mass peaks in fixed target environments were unsuccessful¹⁸. Subsequent experiments attempted to make use of some distinctive

¹⁷J. L. Ritchie et al., Phys. Rev. Lett. 44 (1980) 230

¹⁸W. R. Ditsler et al., Phys. Lett. <u>71B</u> (1977) 451

features of charm production, such as the 'bachelor' pion from $D^* \to D\pi^{19}$. Due to the small Q value (5.7 Mev) of this strong decay, the pion is nearly at rest in the rest frame of the D^* and the background is restricted to a small region of phase space. Prompt leptons were also used to enhance the charm signal from pp $\to c\bar{c}$, with $c(\bar{c}) \to X$, and $\bar{c}(c) \to l + X$ in invariant mass plots²⁰. These experiments had large acceptance corrections and the determination of the cross section depended on the model assumed for charm production.

An additional problem common to both of the above approaches is the nuclear dependence of charm cross sections. These early experiments were usually performed with hadron beams incident on nuclear targets such as beryllium. Proton cross sections were inferred using

$$\sigma_A = \sigma_{proton} A^{\alpha}$$

where A is the atomic number of the target. One expects the exponent α to be 1 for hard scattering of beam and target nucleon constituents (high Q², momentum transfer squared), and 2/3 in interactions at lower Q² where the beam interacts with the whole nucleus. The only measurement of α for charm production comes from the prompt neutrino beam dump experiment by the E613 collaboration at Fermilab²¹ where several target materials were used, and α was measured to be 0.75. However, the inferred proton production cross section (σ_{proton}) is in disagreement with that

¹⁹V. L. Fitch et al., Phys. Rev. Lett. 46 (1981) 761

²⁰R. Bailey et al., Phys. Lett. <u>23B</u> (1983) 237

²¹M. E. Duffy et al., Phys. Rev. Lett. <u>55</u> 1816

derived from measurements made with the bubble chamber used in our experiment.

Furthermore, α has been shown to depend on the momentum of the produced particle in strange particle production²², contrary to the usual assumption that it is a constant. Thus extrapolation of nuclear target data to obtain the desired σ_{proton} appears to be subject to considerable systematic uncertainty.

Mass peak searches were also performed at the ISR. The Lamp Shade Magnet (LSM) detector took quasi elastic proton triggers $pp \to p' + X$ where p' is a quasi elastic proton, and the Split Field Magnet (SFM) took electron triggers $pp \to e^- + X$. These groups reported peaks at 2.3 GeV/ c^2 in the $K^-p\pi^+$ system, corresponding to the Λ_c charm baryon²³.

The observed longitudinal momentum distribution was flat, leading to a production cross section of order 1 mb. These results suffer from very large acceptance corrections and poorly known branching ratios. In both of these ISR experiments the charm hadron must have large longitudinal momentum in order for its decay products to be within the acceptance of the apparatus, and the branching ratio of $\Lambda_c \to K^+ p\pi^-$ is known to no better than 50%.

The third approach to charm production cross sections measurement involves the direct observation of decay vertices in emulsion or bubble chamber targets. Results from emulsion exposures are difficult to interpret, due to the problem of nuclear

²²D. S. Barton et al., Phys. Rev. <u>D27</u> (1983) 2580

²⁸D. DiBitonto, AIP Conference Proceedings No. 85 (1981) 26

dependence mentioned earlier. Experiments using hydrogen bubble chambers include NA27 at the CERN SPS by the LEBC-EHS collaboration, and by our collaboration for experiment E743 at Fermilab. These are experiments with relatively low statistics but clean charm samples. Charm decays are unambiguously identified by their topological signatures in the bubble chamber. Large acceptance corrections are avoided, and cross sections are inferred from topological rather than exclusive branching fractions.

To summarize the situation for cross section measurements, we present in Table 3 a partial list of results; proton-proton cross sections are given, for heavy target experiments, assuming an A^1 nuclear dependence^{24, 25, 26}. These measurements are plotted as a function on the center of mass energy, \sqrt{s} , in Figures 1 and 2. Figure 1 shows the total charm cross section versus \sqrt{s} (only measurements from experiments sensitive to most of the x_F range are plotted) while Figure 2 shows energy dependence of the partial cross section $\sigma(|x_F| > 0.3)$.

Prior to our experiment the situation could be summarized as follows: there was an order of magnitude agreement on the cross section in the 24 to 27 GeV \sqrt{s} energy range, while the ISR results at \sqrt{s} between 53 and 63 GeV implied a dramatic rise in the cross section with increasing energy. Our result at $\sqrt{s} = 39 \, GeV$ indicates a more slowly rising cross section.

²⁴S. Reucroft, Invited Talk at the XXIst Rencontre de Moriond, Les Arcs (1986)

²⁵S. L. Olsen, AIP Conference Proceedings No. 85 (1981) 1

²⁶A. Kernan and G. Van Dalen, Phys. Rep. <u>106</u> (1984) 299

Table 2.3: A partial list of charm cross section measurements; a * denotes experiments which are sensitive only to $|x_F| > 0.3$.

		5 (G T)	, , , , ,
Experiment	Reaction	√s (GeV)	σ (μ b/nucleon)
E595	$\pi^-/Fe ightarrow \mu$	23	17.5+5.5
NA16	p/p o D	26	31.0+16.5
E595	$p/Fe ightarrow \mu$	27	$10.7 \pm 1.1 \pm 1.8$
E613	$\pi^-/W o u$	27	7.8 ± 1.7
NA27	p/p o D	27	34.4 ± 4.2
E743	$p/p \to D$	39	59 ⁺²² ₋₁₅
LSM*	$p/p o \Lambda_c$	53	2400 ± 1000
R408*	p/p o D	53	210 ± 120
R416*	$p/p o \Lambda_c$	62	150 ± 70
R603*	$p/p o \Lambda_c$	62	1800 ± 600
R606*	$p/p o \Lambda_c$	62	1000 ± 400
R606*	$p/p o \Lambda_c$	63	480 ± 200
SFM(CBF)*	$p/p ightarrow \Lambda_c$	63	200 – 1100
SMF(CBF)*	$p/p o D^o$	63	600 — 5000

Figure 2.1: Charm cross section vs. center of mass energy; only measurements from experiments sensitive to most of the x_F range are shown.

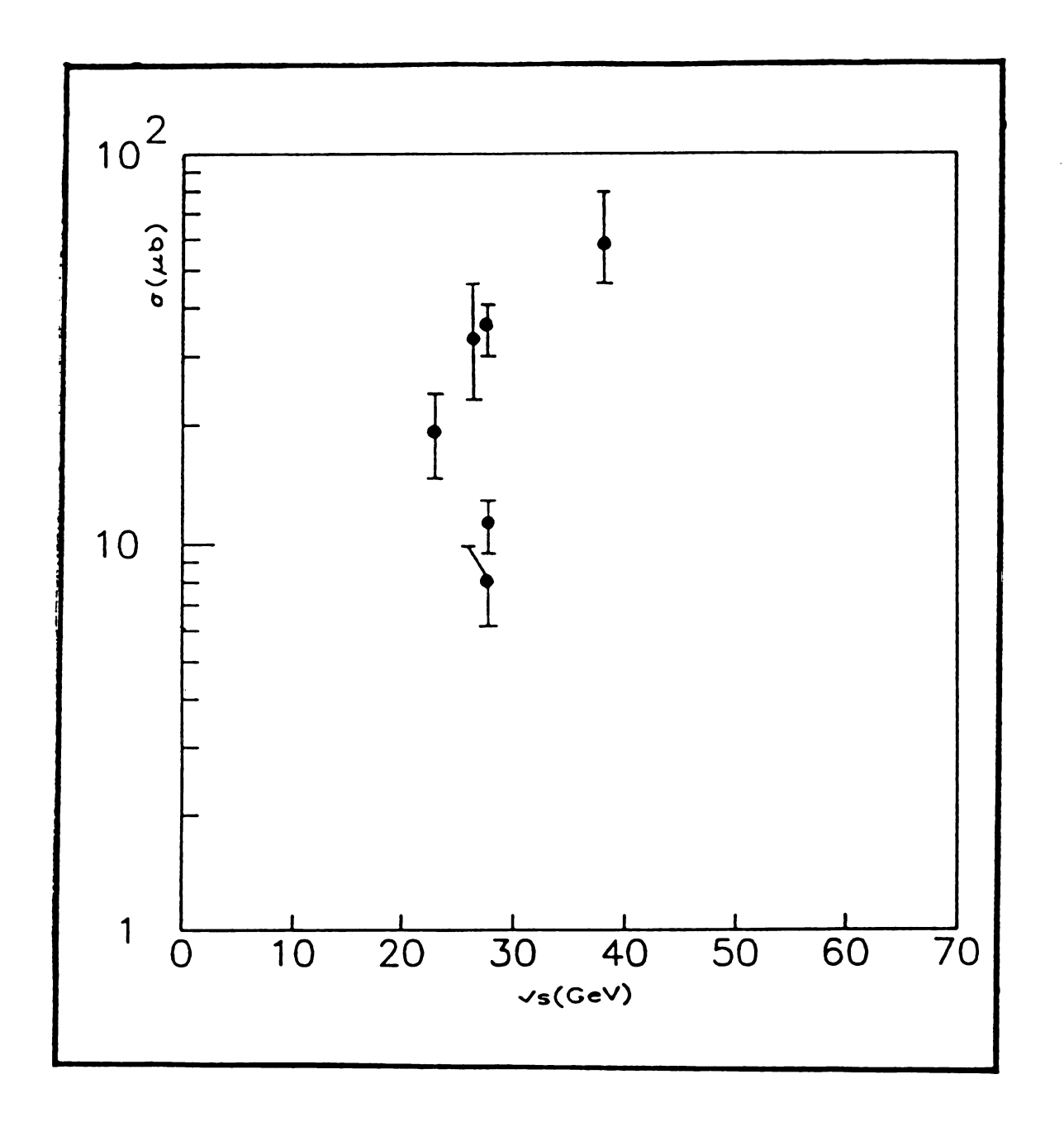
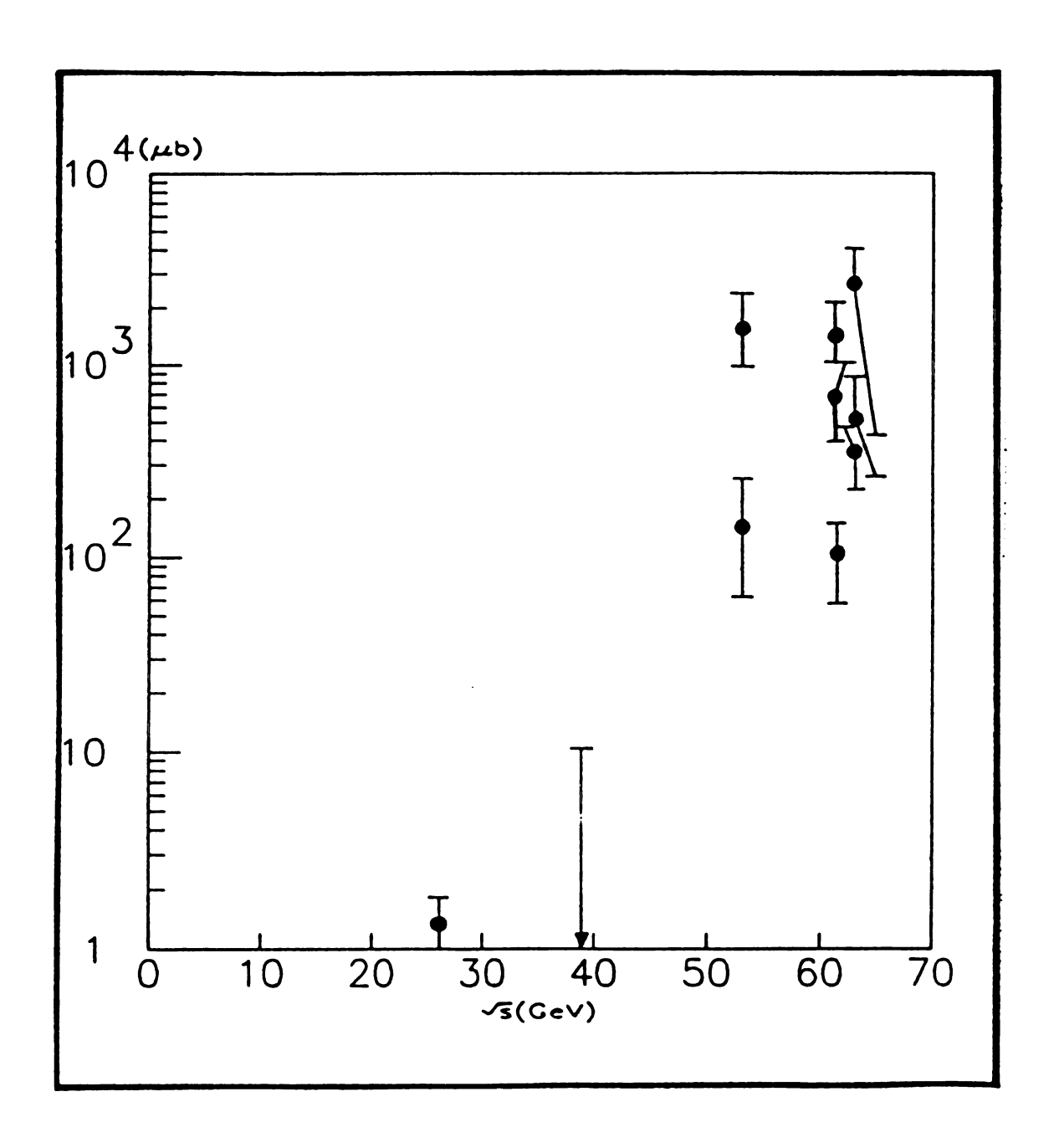


Figure 2.2: Charm partial cross section ($|x_F| > 0.3$) vs. center of mass energy; upper limit at $\sqrt{s} = 39$ GeV is from our experiment.



2.3 Attempts to measure charm differential cross sections in x_F and p_T^2

Several experiments, in a variety of environments, have also attempted to measure the charm differential cross sections in the Feynman variable x_F , the longitudinal momentum fraction of the charm hadron in the center of mass frame of the beam and target, and in the transverse momentum squared p_T^2 . Charm production is often parametrized empirically as

$$\frac{d^2\sigma}{dx_Fdp_T^2} \sim (1-|x_F|)^n exp(-bp_T^2).$$

While in principle the invariant distribution $Ed\sigma/dx_F \sim (1-|x_F|)^n$ should be used, this procedure is not always followed and most experimenters used the non invariant distribution $dN/dx_F \sim (1-|x_F|)^n$ to obtain the exponent n.

There is general agreement on a value of $b \approx 1 \text{ (GeV/c)}^{-2}$, corresponding to an average transverse momentum of 1 GeV/c, independent of the target used, as seen in Table 4. The x_F behaviour of charm production on the other hand is not well understood with results for n, given in Table 4, varying widely, from $n \approx 1$ to $n \approx 10$. Although no systematic trend is evident, in using the data in Tables 3 and 4 one must be aware of the possible distortions in the heavy target data caused by nuclear effects.

2.4 Two mechanisms for hadronic production of charm

Several mechanisms consistent with our current understanding of QCD have been proposed to describe charm production. The quark and gluon fusion and excitation

Table 2.4: A partial list of measurements for the production parameters n and b.

Experiment	Reaction	\sqrt{s} (GeV)	$< p_T > (GeV/c)$	$b(GeV/c)^{-2}$	n
NA11	$\pi^-/Be o D$	19	-	1.1 ± 0.5	0.8 ± 0.4
NA16	p/p o D	26	$\textbf{0.75} \pm \textbf{0.12}$	1.1 ± 0.3	2.8 ± 0.8
E595	$p/Fe ightarrow \mu$	27	0.70 ± 0.15	-	5.0 ± 0.8
NA27	$p/p \to D$	27	-	1.21 ± 0.14	4.8 ± 0.7
E743	p/p o D	39	-	0.66+0.23	11.0+4.6

models describe charm production as a result of relatively hard collisions between hadron constituents, while the intrinsic charm model (ICM), based on the postulation of a valence charm component of hadrons, describes charm production as the dissociation of a charm quark pair from an incident hadron through relatively soft collisions. Determination of charm production cross section and dynamics can provide a sensitive test of both the hard and the soft mechanism.

From the perspective of the hard scattering mechanism, the quark and gluon processes that can give rise to charm hadrons in hadron-hadron collisions fall into two classes: fusion processes and excitation processes²⁷. The fusion processes

$$gg \rightarrow c\bar{c}, q\bar{q} \rightarrow c\bar{c}$$

are illustrated in Figure 3(a). Calculation of these diagrams requires knowledge of

²⁷B. L. Combridge, Nucl. Phys. <u>B151</u> (1979) 429

the valence and sea quark distributions, known as structure functions, of the colliding hadrons. The structure functions of the proton have been measured in deep inelastic lepton-hadron scattering, while the gluon distribution has been inferred from these measurements. The structure functions are usually parametrized as functions of Bjorken x, the fractional momentum of the quark or gluon relative to the parent hadron, and Q^2 , the momentum transfer squared in the collision²⁸.

In the proton-proton collisions examined in this experiment an initial state antiquark can only come from the sea which is peaked at small x. Since the gluon distribution dominates at small x, gluon fusion is expected to dominate over quark fusion in charm production.

Excitation processes, illustrated in Figure 3(b), can be expressed as

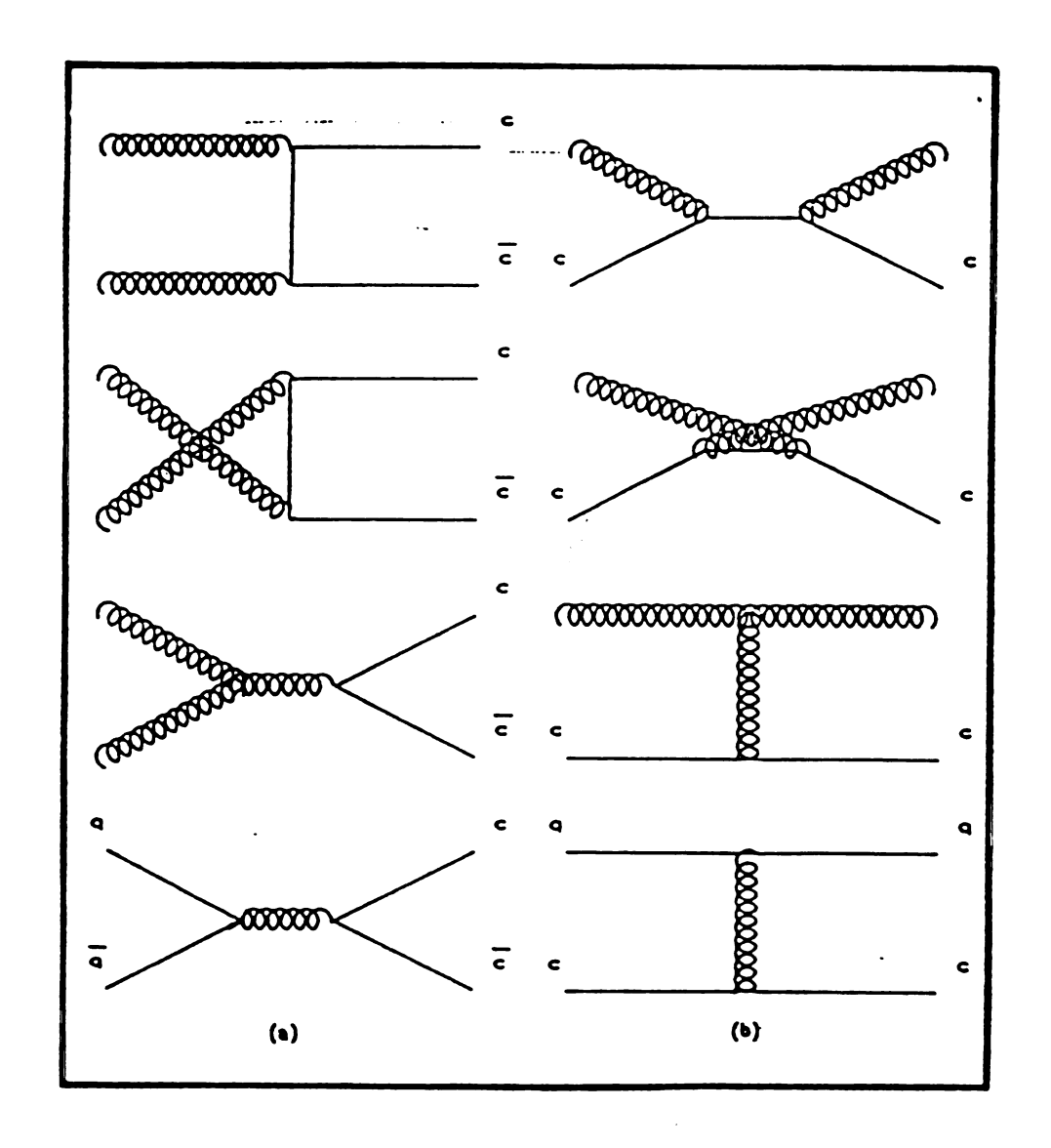
$$gc \to gc, qc \to qc, \overline{q}c \to \overline{q}c,$$

where, in addition to the gluon, up, down, and strange quark distributions, the initial state involves the charm sea in the beam or target. To date no measurements of the charm sea distribution are available, it must be estimated and therefore predictions of contributions to the cross section from excitation processes have correspondingly large uncertainties.

Perturbative QCD gives the Feynman amplitude for quark and gluon level processes. The production cross section for charm pairs is obtained by summing over contributing processes $\hat{\sigma}$ and integrating over allowed momenta, from the production

²⁸E. Eichten, I. Hinchliffe, K. Lane, and C. Quigg, Rev. Mod. Phys. <u>56</u> (1984) 247

Figure 2.3: First order diagrams for the (a) Fusion and (b) Excitation processes.



threshold to the initial state invariant mass,

$$\sigma_{c\overline{c}} = \Sigma_i \int_{s_{th} \leq s \leq s} dx_1 dx_2 \hat{\sigma}_i P(x_1, Q^2) P(x_2, Q^2),$$

The quark gluon process energy is $\sqrt{\hat{s}} = \sqrt{sx_1x_2}$, while the sum extends over all contributing diagrams. Usually the threshold value is taken as the mass of the charm quark pair $(m_c \simeq 1.2\text{-}1.8 \text{ GeV})$ and the momentum transfer squared in the structure functions (P distributions) is taken as $Q^2 \approx 4m_c^2$.

To convert the pair production cross section $\sigma_{c\bar{c}}$ into cross sections for physical hadrons, hadronization schemes are invoked. The simplest scheme is delta function fragmentation. Charm quark fragmentation is assumed to be given by the fragmentation function $f(z) = \delta(z)$, where z is the momentum fraction of the charm hadron relative to the charm quark. A more sophisticated fragmentation scheme is implemented in the LUND Monte Carlo ²⁹.

Due to the dominance of small x values for the gluon and antiquark structure functions in a proton, fusion processes lead to central charm production $(\frac{dN}{dx}$ strongly peaking at x = 0), in proton-proton collisions. Including only the first order processes of Figure 3(a) the charm cross section at our energy, $\sqrt{s} = 39$ GeV, is predicted to be^{30,31}

$$\sigma_{fusion} \approx 30 \mu b$$
,

²⁹T. Sjostrand, Comp. Phys. Comm. 39 (1986) 347

³⁰R. K. Ellis and C. Quigg, Fermilab FN-445 (1987)

³¹C. R. Cudell, F. Halsen, and K. Hikasa, MAD/PH/76

with an energy dependence

$$rac{\sigma_{fusion}(\sqrt{s} = 39 GeV)}{\sigma_{fusion}(\sqrt{s} = 27 GeV)} pprox 2$$

Predictions for the excitation processes are highly sensitive to assumptions made on the charm sea distribution. Recent estimates³² gave

$$\sigma_{\text{excitation}} \approx 2 \times \sigma_{\text{fusion}}$$

at
$$\sqrt{s} = 39 \text{ GeV}$$
.

As the fusion and excitation processes are both hard scattering mechanisms, the energy dependence of the contribution to the cross section from excitation processes is expected to be similar to that of fusion processes. However, as the spectator charm quark is expected to recombine with the beam fragments after the excitation process, a large forward component was predicted for the longitudinal momentum (x_F) distribution³³.

The second, soft scattering, mechanism for charm production involves the hypothesis of intrinsic charm (ICM). In the ICM hadron wave functions are postulated to contain an intrinsic $c\bar{c}$ component distinct from the sea³⁴, so that for a proton

$$|p>=|uudc\bar{c}>.$$

As opposed to charm pairs from the sea, intrinsic charm pairs exist over relatively long time scales appropriate for valence quarks. They have the same velocity as the parent

³²V. Barger, F. Halsen, and W. Y. Keung, Madison preprint DOE-ER/00881-215 (1981)

³³R. Odorico, AIP Conference Proceedings No. 85 (1981) 100

⁸⁴S. J. Brodsky, P. Hoyer, C. Peterson, and N. Sakai, Phys. Lett. 93B (1980) 451

hadron and therefore carry a large momentum fraction, leading to forward production of charm hadrons. In contrast to the hard mechanism of fusion-excitation, production via the ICM should chiefly occur at low momentum transfers, where perturbative QCD is not applicable.

The ICM was proposed following the ISR reports of copious forward charm production. Charm production by this mechanism is diffractive and the model reproduces the large ISR cross sections³⁵

$$\sigma_{intrinsic} \sim 1mb, \sqrt{s} = 60 GeV.$$

A linear interpolation between the ISR values and measurements made at lower energies, e.g. the NA27 results³⁶, would predict a dramatic growth of the cross section over a small energy range,

$$\frac{\sigma_{intrinsic}(\sqrt{s} = 39GeV)}{\sigma_{intrinsic}(\sqrt{s} = 27GeV)} \approx 10,$$

2.5 Summary of the goals and results of E743

Our proposal to measure the energy dependence of hadronic charm production was accepted by Fermilab in December, 1983. The experiment was designed to overcome three major difficulties in the measurement of charm production cross sections: the nuclear dependence of charm production, the insufficient knowledge of exclusive branching ratios, and the poor acceptance of charm decay products in the apparatus.

³⁵S. L. Olsen, AIP Conference Proceedings No. 85 (1981) 1

²⁶LEBC-EHS Collaboration, Berkeley Conf. Preprint, presented by M. E. Michalon and M. Iori

First, the nuclear dependence of charm production is not well understood; a hydrogen bubble chamber target circumvents the problems involved in extrapolating from heavy target cross sections. Secondly, for the purpose of extracting cross sections, exclusive or semileptonic branching ratios for charm are not sufficiently well determined and systematic uncertainties introduced through these branching ratios can be severe; the active target allows us to see the majority of the important decay modes. Lastly, charm production kinematics, i.e. the Feynman x distributions, are virtually unknown; we obtain reliable data on charm hadroproduction via a spectrometer with good acceptance in x_F and p_T .

Our apparatus allowed full reconstruction of charm decay vertices in the rapid cycling, high resolution Lexan bubble chamber (LEBC). Charm decays were topologically tagged during scanning of bubble chamber photographs, charged tracks decaying into three prongs and four pronged decays of neutral tracks are unambiguous charm signatures.

Identification and momentum measurement of charged decay products were provided by the Fermilab Multiparticle Spectrometer (FMPS). In the E743 configuration, the FMPS consisted of a superconducting analysis magnet with a 0.7 GeV/c transverse momentum kick, ten tracking stations, two Čerenkov counters, and a transition radiation detector. The acceptance of the spectrometer was 100% for charged particles with $x_F \geq 0$.

During the third run of Tevatron II (spring and summer 1985), LEBC was exposed to 800 GeV/c primary protons from the Fermilab MT beam line and over

one million minimum bias triggers were taken.

The most fundamental result is an unambiguous measurement of the D meson inclusive cross sections³⁷,

$$\sigma(D/\overline{D}, \sqrt{s} = 39 GeV) = 59^{+22}_{-15} \mu b,$$

with

$$\sigma(D^+/D^-) = 33 \pm 7\mu b, \sigma(D^o/\overline{D}^o) = 26^{+21}_{-13}\mu b.$$

When compared with measurements made at lower energies, such as the D cross section from experiment NA27 at the CERN SPS³⁸, our value of the cross section indicates a weak energy dependence,

$$\frac{\sigma(D/\overline{D}, \sqrt{s} = 39GeV)}{\sigma(D/\overline{D}, \sqrt{s} = 27GeV)} = 1.7^{+0.6}_{-0.5},$$

in disagreement with the strong energy dependence implied by measurements made at the ISR and, correspondingly, with no need for an intrinsic charm component in the nucleon.

Our fit of the longitudinal and transverse momentum distributions of observed

D meson decays yield

$$\frac{d\sigma}{dx_F} \sim (1 - |x_F|)^n, n = 11.0^{+4.6}_{-3.6},$$

and

$$rac{d\sigma}{dp_T^2} \sim exp(-bp_T^2), b = 0.66^{+0.23}_{-0.20} (Gev/c)^{-2}.$$

³⁷R. Ammar et al., Phys. Lett. <u>B183</u> (1986) 110

²⁶LEBC-EHS Collaboration, Berkeley Conf. Preprint, presented by M. E. Michalon and M. Iori

The predominantly central Feynman x distribution we observed is, like the inclusive cross sections reported above, also inconsistent with the predictions of the ICM.

A more generally accepted model for charm hadronic production is the Fusion model (FM), based on perturbative QCD. It is assumed that in proton-proton collisions the major contribution to the charm cross section comes from first order processes involving the combination of a pair of gluons to form a $c\bar{c}$ pair. The FM prediction

$$rac{\sigma(D/\overline{D},\sqrt{s}=39GeV)}{\sigma(D/\overline{D},\sqrt{s}=27GeV)}\simeq 2$$

is in good agreement with our result, although the FM prediction for the total charm cross section is smaller than the experimental value by a factor $K\simeq 2$. This discrepancy can be attributed to the fact that higher order QCD diagrams have not been included in the calculation. The energy dependence is not expected to change significantly with the inclusion of second order diagrams, thus the agreement with the FM prediction should be maintained.

Also measured are the associated charged multiplicity in both charm and noncharm events. For charm events the mean primary multiplicity was³⁹

$$< N_{ch} > = 11.9 \pm 1.0, pp \rightarrow charm + X$$

while for inclusive proton-proton events

$$< N_{ch} > = 10.26 \pm 0.15, pp \rightarrow X.$$

We note that very few charm particles were observed in the low multiplicities. We

³⁰ R. Ammar et al., Phys. Lett. <u>B178</u> (1986) 124

can attempt to compare our associated multiplicity with all non-diffractive collisions by removing the multiplicities which are dominated by the diffractive component $(N_{ch}=2,4,\sim 6 \text{ mb})$ from the inclusive multiplicity distribution. This yielded a non-diffractive multiplicity of $< N_{ch,non-diffractive}>= 11.59 \pm 0.16$, which is rather close to that observed in charm associated events.

In the next two chapters we shall give a detailed description of our apparatus (Chapter 3) and of our procedures for data reduction and analysis (Chapter 4). Chapter 5 describes our study of the trigger bias as well as our results for the inclusive multiplicity distribution. Chapters 6 and 7 give detailed results on the D meson total and differential cross sections. In Chapter 8 we compare these experimental results with predictions by the FM and other, unusual, mechanisms for charm hadroproduction. Finally, a summary of the results presented in this thesis will be given in Chapter 9.

Chapter 3

EXPERIMENTAL APPARATUS

This chapter gives detailed descriptions of the apparatus of experiment E743.

3.1 The beam and beam optics

During the third run of the Fermilab Tevatron II, our bubble chamber was exposed to 800 GeV/c primary protons from the accelerator. Figure 1 illustrates the optics of the MT beam line and the site map of Figure 2 shows the beam line location. To accommodate the low rate capabilities of the bubble chamber, the beam was attenuated by a four foot beryllium block. Initial collimation of the attenuated beam was performed by a remote-controlled collimator. A kicker magnet with 0.8 GeV/c transverse momentum kick downstream of this collimator prevented protons from entering the bubble chamber before it became sensitive. Two additional collimators, five dipole magnets, and two quadrupole magnets downstream of the kicker provided final beam tuning.

At the bubble chamber the 800 GeV protons were attenuated to a mean incident

Figure 3.1: Optics of the MT beam line.

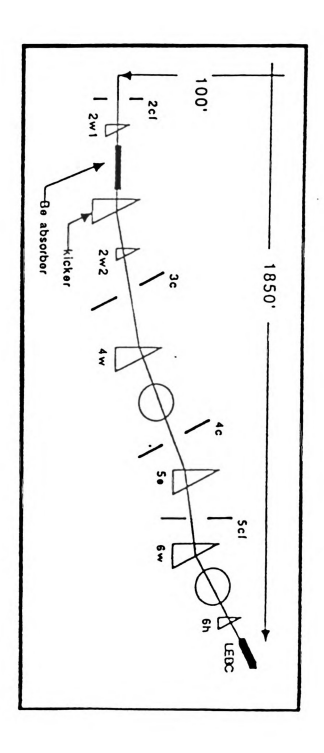
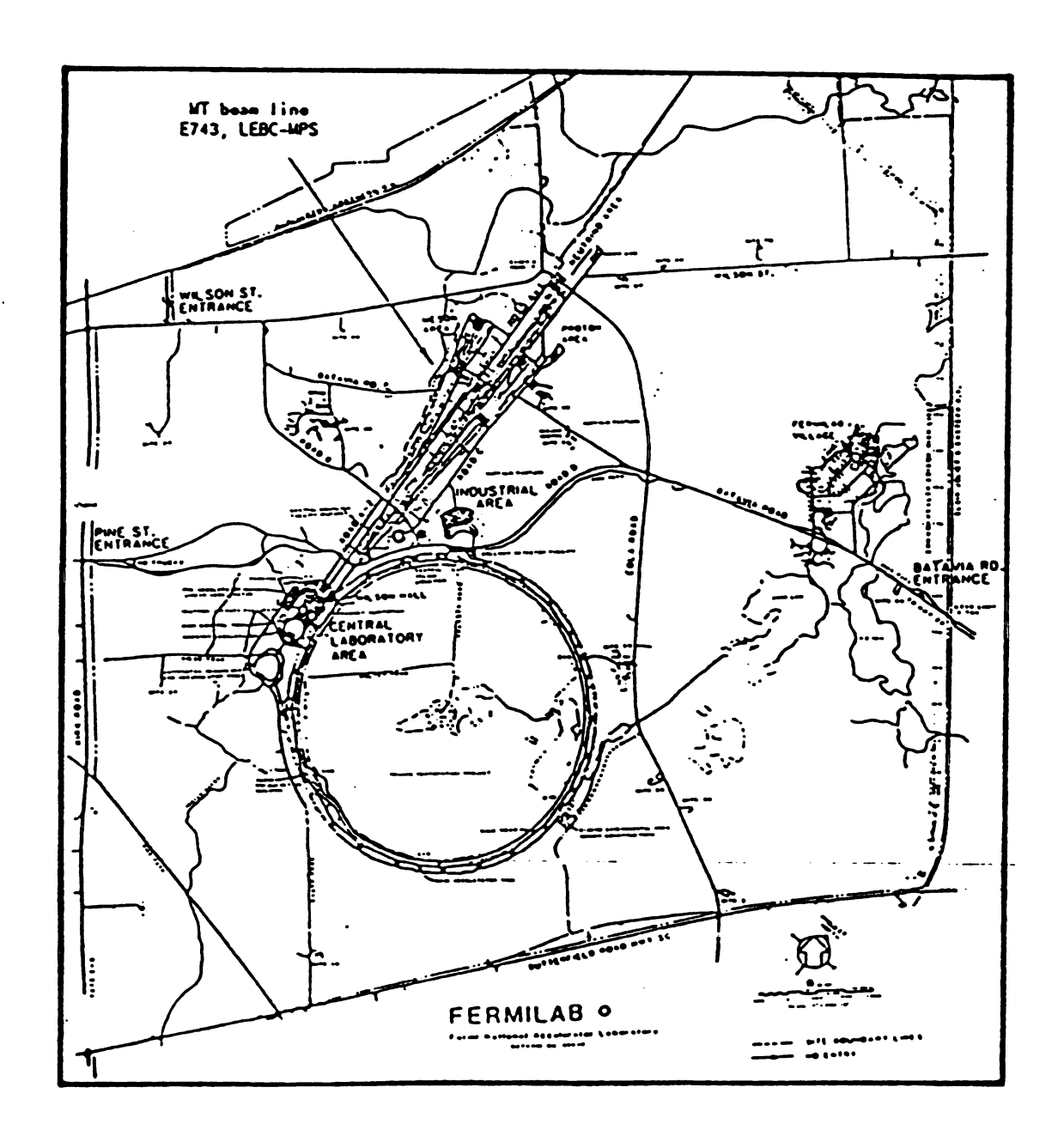


Figure 3.2: Site map showing the location of the MT beam line.



rate of 1.5×10^4 per accelerator spill and collimated to an 8 mm vertical by 1 mm horizontal spot. The spills were 20 to 23 seconds in duration, with 57 to 120 seconds between spills.

The beam was defined, prior to entering the bubble chamber, by three stations of wire planes at 1 mm pitch, approximately one meter apart; the last station was approximately one meter upstream of the bubble chamber. In addition there were six scintillators between the last beam wire station and the bubble chamber, four of which further defined the beam and two vetoed beam halo. These scintillation counters were part of the trigger system.

During the running period a total of 1.18×10^6 bubble chamber photographs were taken with a minimum bias trigger (see section 3.4). Subsequent scanning of these photographs revealed about 5×10^5 recorded proton-proton interactions. Results reported in this thesis are derived from the first analyzed 25% of the data, corresponding to an experimental sensitivity of

$$s = 3.5 \pm 0.1 events/\mu b$$
.

In addition 8.1×10^4 photos were taken with an unbiased trigger for multiplicity and trigger efficiency studies. Scanning these photos revealed 1.6×10^4 recorded proton-proton interactions.

3.2 LEBC, the hydrogen target and vertex detector

Figure 3 is a photograph of the Lexan Bubble Chamber (LEBC). LEBC is a high resolution, rapid cycling hydrogen bubble chamber designed to study short lived particles. Table 1 shows the most relevant parameters for LEBC. The main body of the chamber was milled from a single slab of the thermoplastic polycarbonate Lexan. The beam entry and exit windows, and the flexible expansion membrane were glued to the main body using a solvent cementing technique which ensured secure sealing at cryogenic temperatures. A heat exchanger and a filling valve mounted on top of the main body maintained chamber temperature and pressure. The expansion membrane was driven by a piston with 0.5 mm stroke. The chamber assembly was housed in a steel vacuum tank. Figure 4 is a beam's eye view of the chamber assembly, Figure 5 shows the vacuum tank and camera set up. Greater details for the specifications of LEBC can be found elsewhere.

In order to achieve high resolution, small bubble size and high bubble density were required. For the bubble size to be small the expansion cycle must be short, so as not to allow time for the bubbles to grow too large. The cycling rate also must be high in order to achieve acceptable data rates. Due to the demand of rapid cycling, the fiducial volume must be made small. Since the short lived particles of interest were expected to decay near their production vertex, a small fiducial volume was acceptable. Mechanical integrity dictated that the entire chamber be constructed of lexan,

¹I. L. Benichou et al., Nucl. Instr. and Meth. <u>190</u> (1981) 487

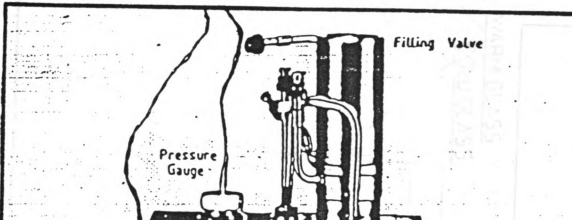


Figure 3.3: A photograph of our LExan Bubble Chamber.

Exit Window

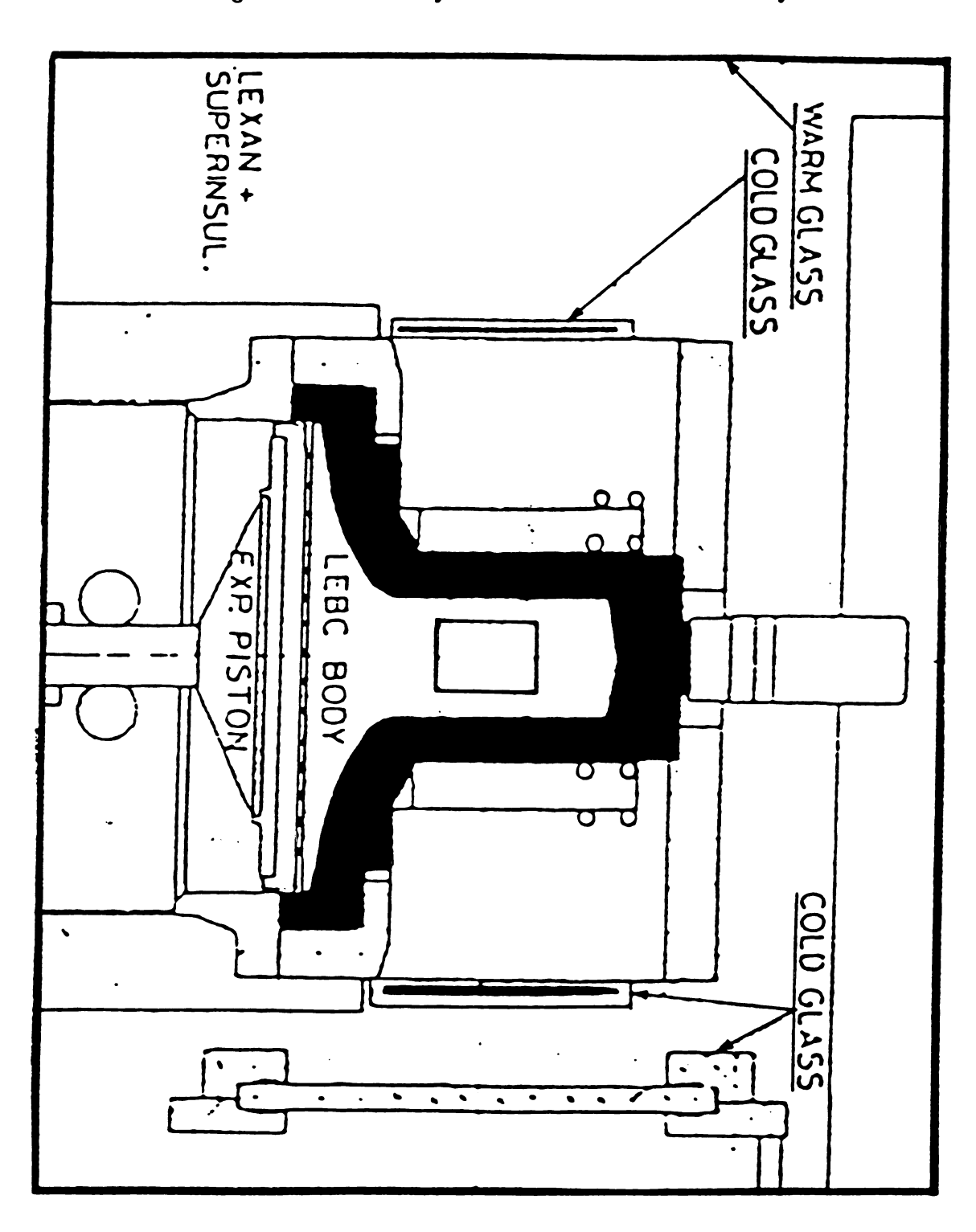


Figure 3.4: Beam's eye view of the chamber assembly.

Pund of the CAMERA Cassetts

Figure 3.5: Vacuum tank and camera set up for LEBC.

a thermoplastic polycarbonate with high impact strength at cryogenic temperatures.

Lexan has the further advantage of being transparent to visible light.

Figure 6 shows the optical system for LEBC. The resolution R of two point objects is limited by diffraction, $R=1.22\frac{\lambda}{a}$, where λ is the wavelength of the light source and a is the lens aperture. The depth-of-field δ is proportional to the square of the resolution, $\delta \approx 5R^2$. High resolution therefore implies limited depth-of-field. The optical system must be able to resolve individual bubbles, whose size was $\approx 20\mu\text{m}$. During data taking a resolution of $20\mu\text{m}$ was achieved for the film image of the bubbles, with a 2 mm depth-of-field.

Monochromatic illumination by a pulsed dye laser was chosen to circumvent problems of chromatic aberrations, and correction lenses were used to eliminate distortions of the image by the cold window of the vacuum jacket and the lexan chamber body. Photographs were taken in two conventional camera views $\pm 6.5^{\circ}$ from vertical. A pair of optical fibres guided the laser light to condensor lenses focussed at the camera apertures.

3.3 The FMPS spectrometer

In the E743 configuration, the Fermilab Multiparticle Spectrometer (FMPS) consisted of one superconducting analysis magnet giving a 0.7 GeV/c transverse momentum kick in the horizontal plane, ten tracking stations, two Čerenkov counters, and one transition radiation detector. The analysis magnet was positioned approximately

Figure 3.6: The optical system of LEBC.

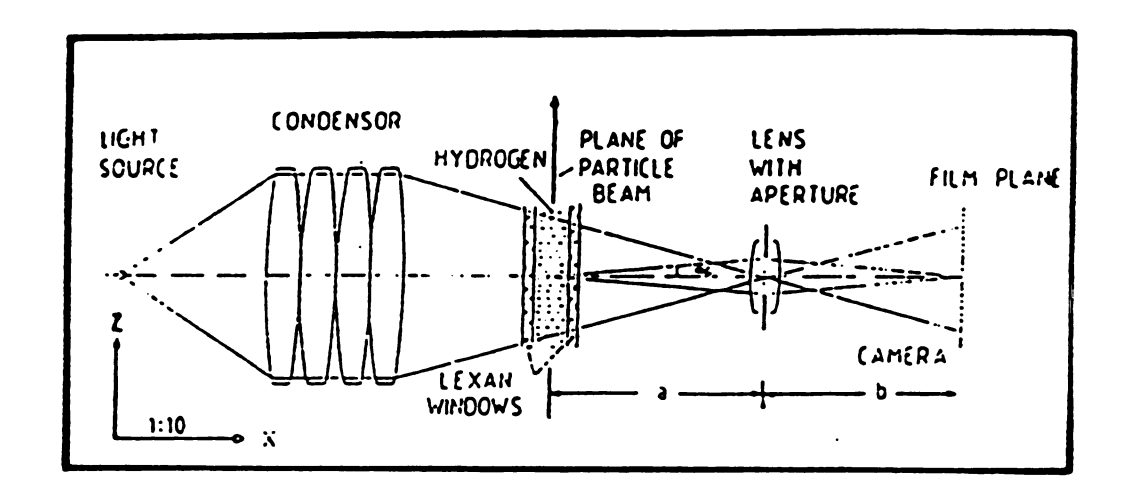


Table 3.1: Important LEBC parameters.

Material	$(H_{14}C_{16}O_3)_n$
Cycling rate	30 s ⁻¹
Cycle duration	5 <i>ms</i>
Live time	500μs
Fiducial volume	$50\times70\times109mm^3$
Operating T, p, ρ	$29^{\circ}K, 4.2kgcm^{-2}, 0.057gcm^{-3}$
Stereo angle	±6.5°
Illumination	500 nm dye laser, 200 ns pulses
Mean bubble diameter	20μm
Mean bubble density	70 <i>cm</i> ⁻¹

three meters downstream of the chamber. The magnet apertures were 84 cm in the vertical plane and 122 cm in the bend plane, corresponding to an angular acceptance of ± 150 milliradians in the vertical plane. The momentum resolution was

$$\frac{\Delta p}{p}(p=100GeV/c)=1.5\%$$

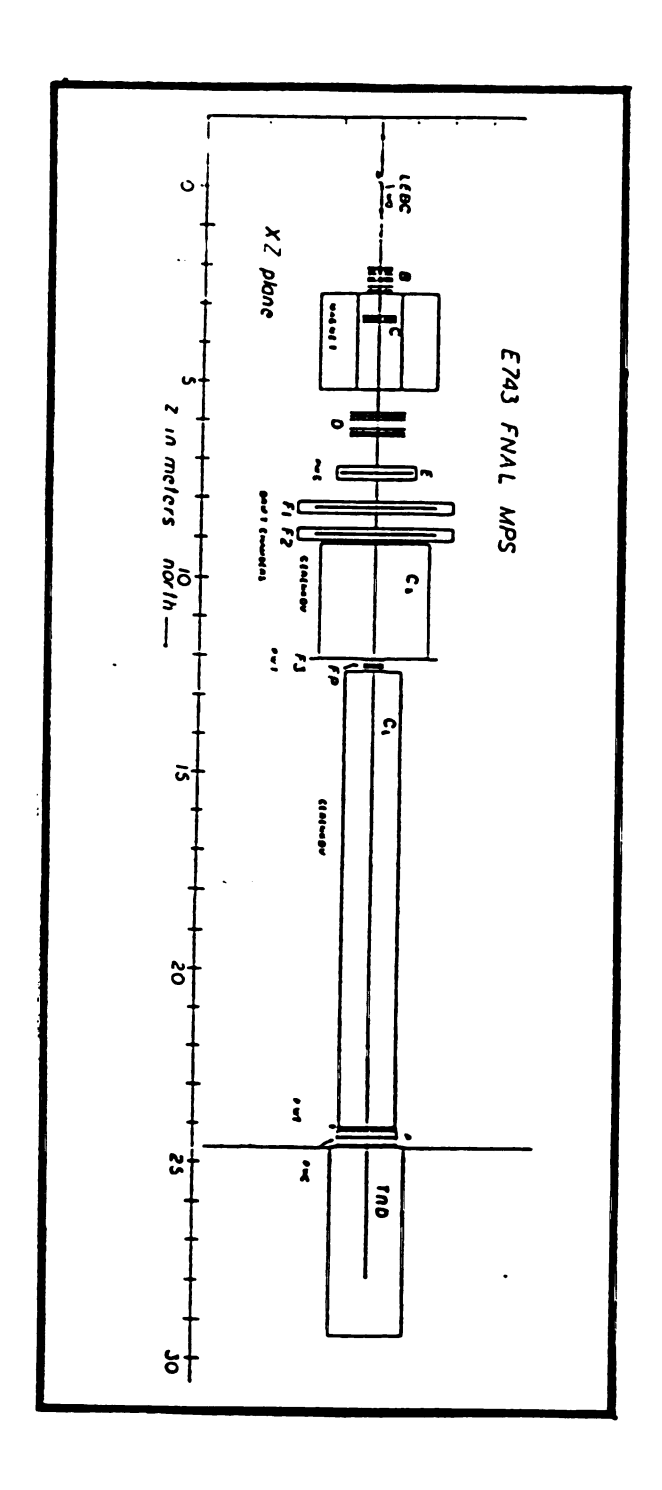
for tracks within the aperture of the last tracking station, and 2.5% for wider angled tracks. The low momentum threshold for tracks to survive bending by the magnet was 3 GeV/c.

Figure 7 is an elevation view of the FMPS. There were twelve proportional wire planes in the upstream lever arm of the spectrometer. The downstream arm had twelve proportional wire planes, eight drift planes, and four planes of proportional tubes. The four wire planes in the first MWPC station immediately behind the bubble chamber had 0.5 mm wire spacing and was also part of the trigger logic. The remaining MWPC planes had wire spacings between 2.0 mm and 2.5 mm, giving a resolution of ≈ 0.8 mm. The proportional wire stations were filled with a mixture of argon and 20% CO₂.

The two drift stations were operated in common stop mode. At 19 mm pitch, these drift planes had 350 μ m resolution and provided precision track points for the downstream pattern recognition. The drift chambers were filled with a mixture of argon and ethane.

The FMPS was also equipped with two identical stations of proportional wire tubes. Each station consisted of one horizontal and one vertical plane, with a sensitive

Figure 3.7: Elevation view of the Fermilab Multiparticle Spectrometer in the E743 configuration.



area of 365 cm horizontal × 158 cm vertical. Proportional tube cells were 2.5 mm wide. Except when cells were multiply hit, the proportional tubes provided three dimensional hit coordinates by the method of charge division. These hit coordinates aided view matching of tracks during pattern recognition. For the ordinary coordinate the resolution was 7.3 mm while for the charge division coordinate the resolution was 1.5% of the length of the proportional tube wire. The proportional tube stations were also filled with argon CO₂.

Approximately four meters downstream of the magnet was a nitrogen filled Čerenkov counter with pion, kaon, and proton momentum thresholds (for a given particle, the counter does not respond unless the particle momentum exceeds the threshold p_{th})

$$p_{th}(\pi/K/p) = (5/25/38)GeV/c.$$

The second Čerenkov counter positioned seven meters downstream of the magnet was filled with helium, with

$$p_{th}(\pi/K/p) = (17/59/112)GeV/c$$

momentum thresholds. Behind the last tracking station was the transition radiation detector. It consisted of alternating planes of xenon filled proportional wire detectors and carbon fibre radiators.

3.4 The triggers and data acquisition system

The trigger system consisted of six scintillator hodoscopes and four planes of 0.5 mm pitch proportional wires, illustrated in Figure 8. Four scintillators positioned upstream of the bubble chamber signalled the arrival of the beam. Two additional scintillators approximately 20 cm in front of the bubble chamber and away from the beam spot vetoed beam halo. Two vertical and two horizontal wire planes downstream of the chamber counted outgoing tracks.

Figure 9 shows the timing of our trigger. At the beginning of an accelerator spill, a kicker magnet pulse swept away incident protons as the bubble chamber expansion cycle started. As the chamber became sensitive, beam was allowed into the fiducial volume and activated the trigger. The trigger turned on the laser flash, which was delayed to allow bubbles to grow to photogenic size.

The bulk of the data for charm studies was taken with a minimum bias, or 'interaction' trigger, defined as 'beam' and at least three tracks in the wire planes. Some data was also taken with an unbiased, or 'beam' trigger, defined by the six scintillators alone, for inclusive physics studies as well as for studies of the interaction trigger bias.

The trigger also activated spectrometer data acquisition. The data acquisition system was based on the Fermilab package MULTI². Detector channels were read out from CAMAC crates by a Jorway 411 branch driver controlled by a PDP-11. From

²V. White, B. Burch, K. Eng, P. Heinicke, M. Pyatetsky, D. Ritchie, Fermilab PN-183 (1983)

Figure 3.8: The E743 trigger system.

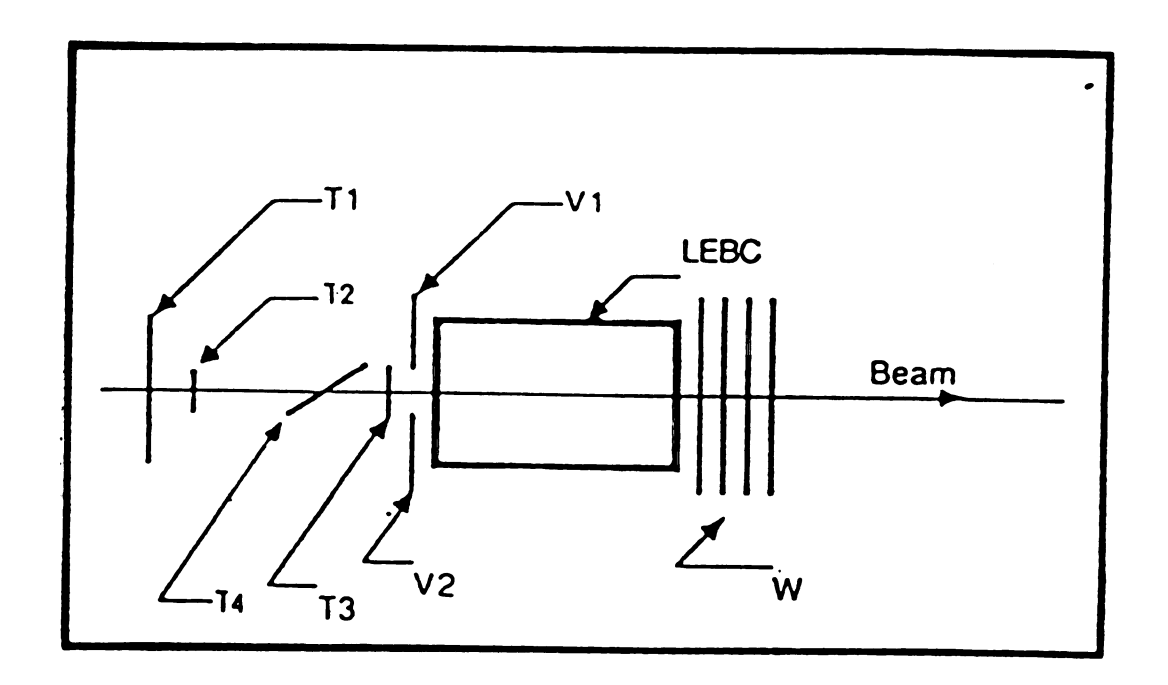
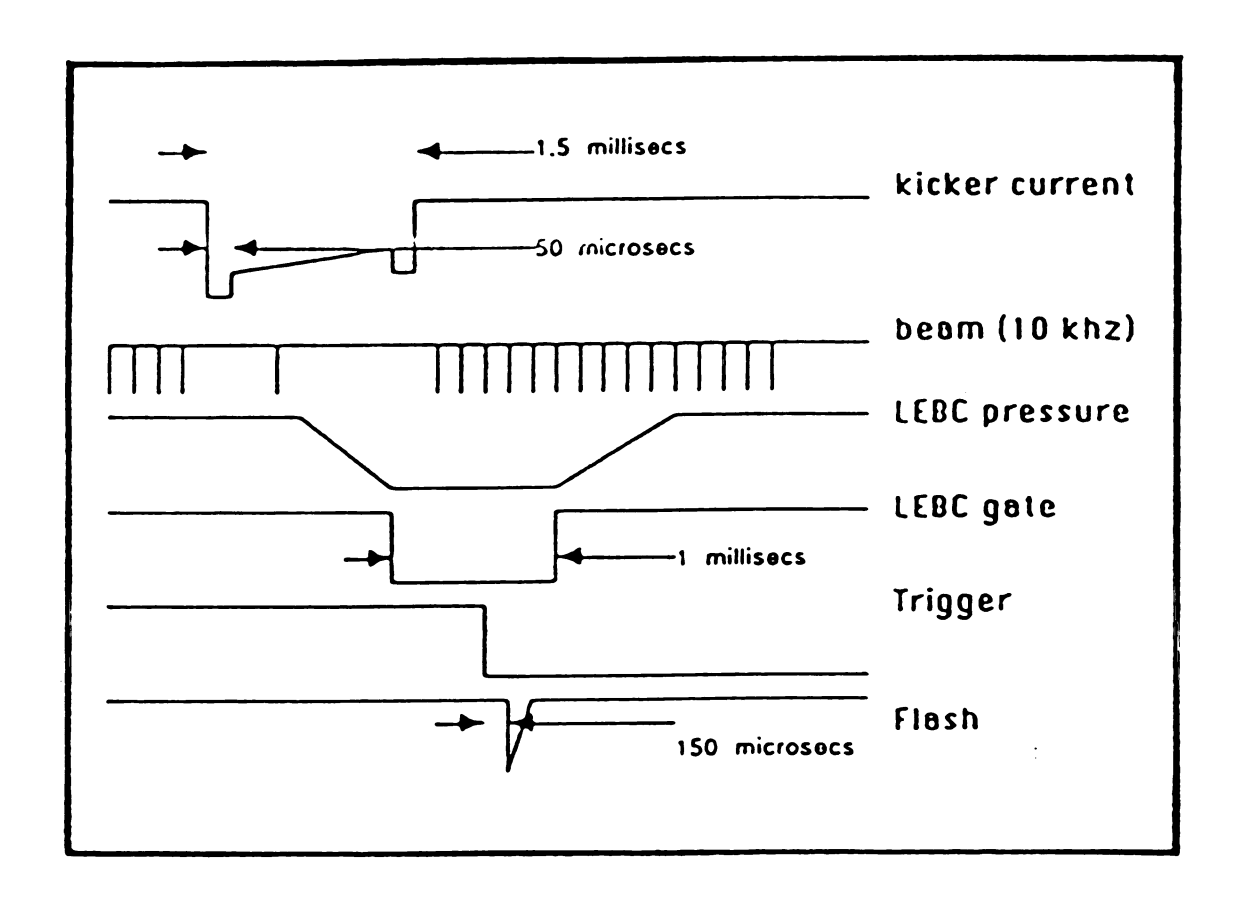


Figure 3.9: Timing of our interaction trigger.



there the event data was packed into a half word integer vector for transmission by a pair of DR11 controllers linking the PDP-11 with a VAX 780. From the VAX, the data was available for logging to magnetic tape, for on-line monitoring, for graphical display, and for partial on-line analysis with specialized user routines.

In the next chapter we shall give detailed descriptions of the procedures followed in our reduction and analysis of the data.

Chapter 4

DATA REDUCTION

We discuss at length in this chapter the procedures followed in reducing and analyzing the data.

4.1 Film analysis

Initially, bubble chamber and spectrometer information were separately processed in two independent data streams. Identification of charm events took place during the scanning and measuring of the bubble chamber photographs. The charm candidate digitizations were stored on magnetic tape in a HYDRA¹ data structure. Spectrometer information for selected events was then analyzed and concatenated to the data structure for further consideration. We describe first the various aspects of film handling.

¹R. Bock et al., HYDRA Topical Manual, CERN Program Library (1981)

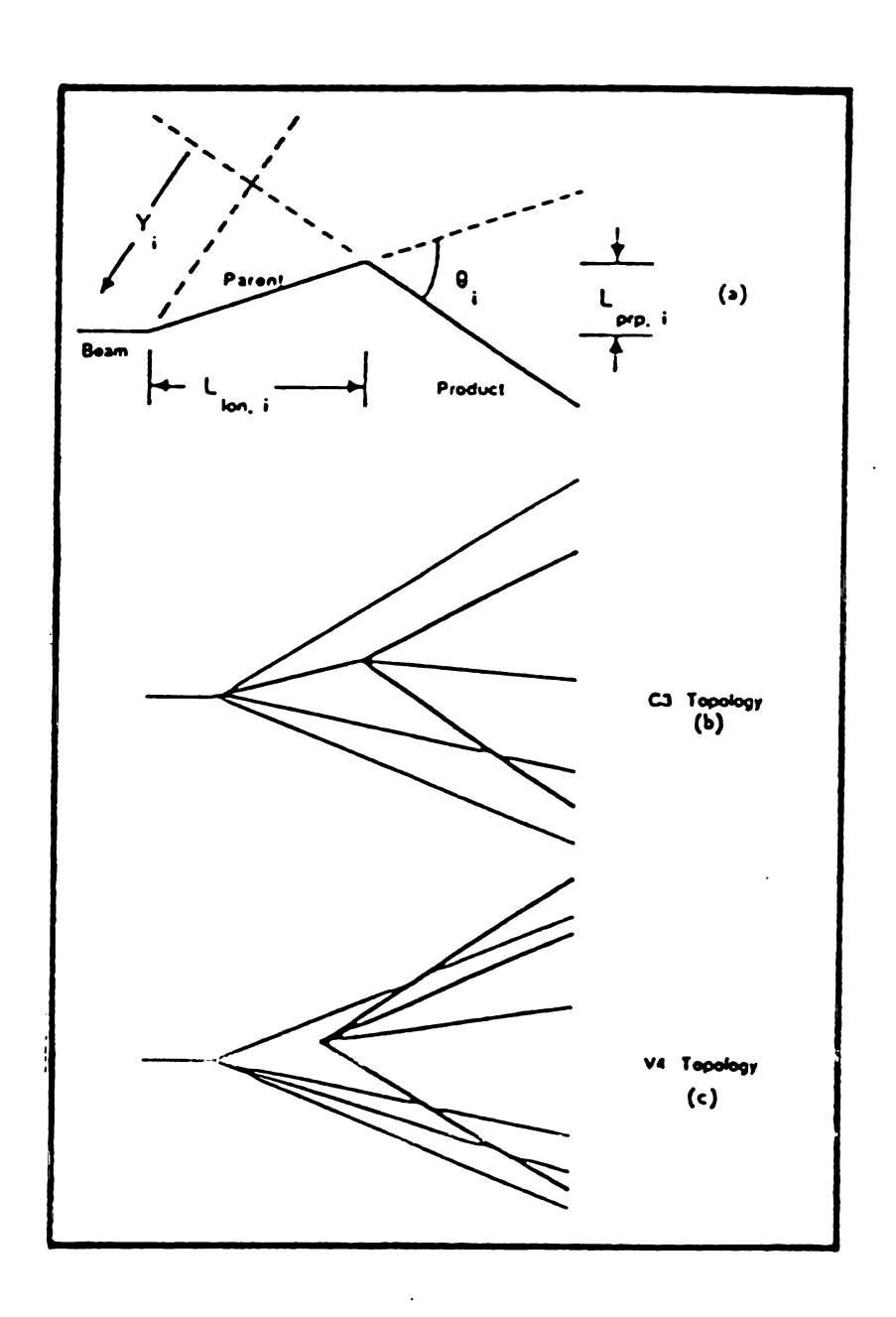
4.1.1 Scanning

The bubble chamber pictures were recorded on fifty millimeter film. After development the film was distributed to scan shops of institutions in our collaboration (50% of the film was scanned at Fermilab under the author's direction). Both views of the bubble chamber were scanned for interactions of interest. Scanning was guided by an upstream measurement of the beam track that generated the trigger. The primary interaction was located and secondary activities were searched for. Secondary vertices were categorized according to their charge multiplicity and by the vertex type. Figure 1 illustrates important decay topologies and parameters. A vertex was of type 'C' if it came from a charged primary track, and 'V' if it came from a neutral track. Thus, for instance, the topology of a $D^+ \to K^-\pi^+\pi^+$ is 'C3'. A second scan was made of the frames in which a proton-proton interaction was observed, looking specifically for secondary activity indicative of charm decay.

Charm decays have topologies C-odd or V-even. As charm particles are short lived and therefore have short transverse flight paths, only those decays which occurred within the 'charm box', a space cylinder 2 mm in radius centered on the interacting beam track, were considered.

In spite of the relatively high multiplicity and the collimation of tracks at our energy, the efficiency for detection of secondary activity was high. The detection of secondary activity in scanning is dependent only on the impact parameter

Figure 4.1: An illustration of (a)important decay parameters and of the charm topologies (b)C3 and (c)V4.



of secondary tracks, where L is the separation between the primary and secondary vertices and θ is the angle between the secondary track and its parent track.

When the daughter is emitted normal to the parent line of flight in the parent rest frame (denoted by the superscipt *), the components of the daughter momentum along and normal to the parent line of flight in the laboratory frame are $q_{\perp}=q^*$, $q_{||}=\gamma\beta e^*$. In the limit of large Q values ($e^*\simeq q^*$), the daughter momentum in the laboratory is approximately $q_{||}\simeq\gamma\beta q^*$, and the decay angle in the laboratory frame is $\sin\theta=\frac{q_{\perp}}{q}\simeq\frac{1}{\sqrt{1+(\gamma\beta)^2}}$; in the limit of a large Lorentz boost from the parent rest frame to the laboratory ($\beta\simeq 1$, $\gamma\gg 1$),

$$\sin\theta\simeq\frac{1}{\gamma}.$$

The decay angle in the laboratory frame decreases as γ^{-1} . On the other hand, the decay length

$$L = \gamma \beta c \tau \simeq \gamma c \tau$$

(τ is the proper decay time) grows as γ , so that the impact parameter is $Y \simeq c\tau$, independent of γ , i.e. the parent momentum.

A more complete treatment (see Appendix A) shows that for all angles of emission, the impact parameter of decay tracks is independent of the parent momentum for sufficiently high Q values and sufficiently large Lorentz boosts from the parent rest frame to the laboratory frame. The mean impact parameter is proportional to the mean life of the parent, with small variations from one decay mode to another.

Figure 2 shows the magnified film image of a charm associated event. After

the film had been double scanned by scanners, charm candidates were selected for measurement by physicists in a third scan of those events tagged as having secondary activity during either of the two previous scans.

In comparison with data taken with this bubble chamber at lower energies, scanning of these events suffered from the increased multiplicity and collimation of tracks but benefitted from the Lorentz boost of decay lengths. On the scanning table, impact parameters were detected by viewing the magnified film image at glancing angle. Our scanners placed themselves at eye level with the table onto which the film image was projected. From this perspective, tracks that did not point back to the primary vertex were easily detected. With some visual aid, for instance by placing a straight edge along the secondary track, non pointing tracks with impact parameters greater than 100 μ m were spotted without difficulty.

Both of the two independent scans were done in the above manner. Double scanning also allowed us to measure the scanning efficiency. Single and double scan efficiencies were defined as follows. If $N_i \equiv \text{number of events found in the } i^{th} \text{ scan}$, and $N_{12} \equiv \text{number of events common to both scans}$, then the efficiency for the two scans is

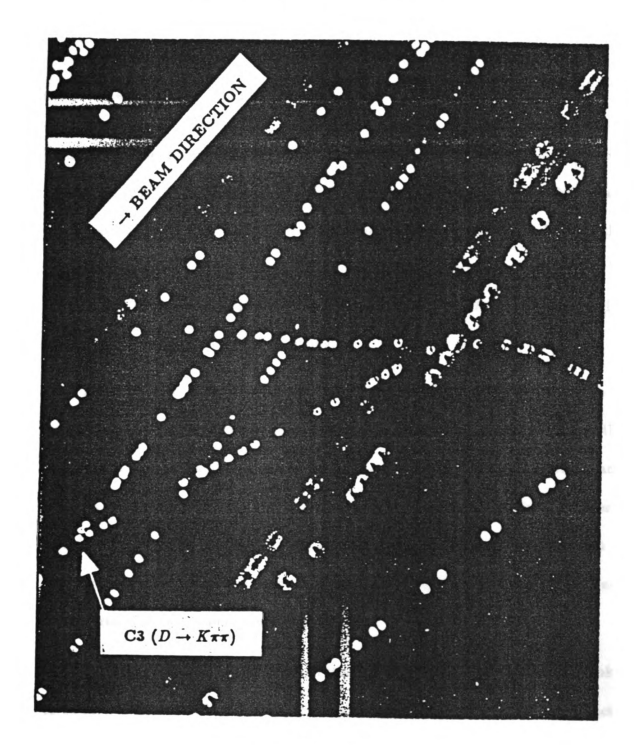
$$\epsilon_1 = \frac{N_{12}}{N_2}, \epsilon_2 = \frac{N_{12}}{N_1},$$

and the double scan efficiency is

$$\epsilon=1-(1-\epsilon_1)(1-\epsilon_2).$$

Our double scan efficiency for the detection of secondary activity was $\epsilon = (90 \pm 5)\%$.

Figure 4.2: Photograph of a charm event.



Events with secondary activity were tagged for the third scan. During this scan secondaries with interesting topologies, C-odd or V-even, were selected as potential charm candidates and sent on for measurement.

4.1.2 Measuring

Film measurement was performed using the Electron Ray Scanning and Measuring Equipment (ERASME) system at CERN. The film was slice scanned with a light beam which passed through the film and was detected in a photomultiplier. A jump in the light intensity at a track bubble caused the position of the bubble to be recorded. In this manner, track points were measured with an accuracy of 2.7 μ m and track angles and vertex positions were found by fitting.

In addition to decay lengths and impact parameters, the dip and ϕ angles of bubble chamber tracks were also measured for the purpose of hybridization, i.e. the matching of bubble chamber tracks to tracks found in the spectrometer. The dip and ϕ angles were defined as $\lambda \equiv \text{(dip)}$ angle between the track and the plane transverse to the beam direction $(-\pi/2 \le \lambda \le \pi/2)$, and $\phi \equiv \text{angle}$ between the projection of the track onto the transverse plane and the beam direction $(0 \le \phi \le 2\pi)$. Track images from the two camera views were matched by their bubble pattern.

The film measurements for selected charm decays were stored in HYDRA banks, to be later concatenated with the spectrometer information on their decay products.

4.2 Event reconstruction

In order to determine the identity of the particles and their decay modes the spectrometer information on the momentum and mass of the decay tracks was analyzed. A pattern recognition program was used to analyze the spectrometer tracking system, followed by steps to combine the bubble chamber and spectrometer information, and to fit the events to kinematical hypotheses. A final pattern recognition stage using graphical software developed by the author was used to recover a significant fraction of those events which would otherwise have been lost. The details of these steps are provided below.

4.2.1 Spectrometer tracking

The program FLOWERS² was used for tracking. FLOWERS was a conventional finder-fitter in four views, with user defined road chambers. The four views were $x_u \equiv \text{bend (horizontal) plane upstream of the magnet,}$

 $x_d \equiv \text{bend plane downstream of the magnet,}$

 $y_u \equiv \text{upstream vertical and slant planes},$

 $y_d \equiv$ downstream vertical and slant planes.

Several passes were made for each event. In each pass the x projections were found first. The y projections were then found and matched to the x projections.

Downstream tracking was performed first, as the greater track separation there facil-

²J. H. Goldman, E623 internal note

itated pattern recognition. View matching was done using charge division hits from the proportional tubes when appropriate, otherwise hits on slant planes were used. Bubble chamber measurements of the position of the primary vertex aided upstream tracking.

A distinct set of road chambers pertained to each pass. Road chambers were selected to cover both large and small angled tracks and redundancy was built into the selection to cover chamber inefficiencies. Track candidates were selected on the basis of the number of hits and the goodness of fit.

4.2.2 Hybridization and kinematic fitting

Spectrometer tracks found by FLOWERS were at this point hybridized with tracks found in the bubble chamber. Bubble chamber tracks were matched with spectrometer tracks on the basis of their dip and ϕ angles, allowing the identification of charm decay tracks in the spectrometer. The program GEO743 ³ then performed kinematic fitting of hybridized decay tracks.

Under the assumption that all of the decay products were charged, kinematic fits of charm decays were divided into constraint classes. For each decay, energy and momentum conservation gave four equations with four unknowns, the four-momentum of the parent particle. The angles of all charged tracks were measured on film so that, when momentum measurements were available for all decay products, there were three constraints on the fit. This case was termed a 3C (three constraint) fit. When one

³J. W. Waters, E743 internal note

charged decay product was not reconstructable in the spectrometer its angles are still measured on film. There remained only two constraints and the fit was a 2C. With two missing charged decay tracks the fit was a 1C.

If, on the other hand, there is a missing neutral particle (e.g. a π^o or K^o) then, even when all the charged decay products were measured, there are no constraints on the kinematics. A OC calculation of the parent momentum p_D can be made for any assumption regarding the parent and missing neutral daughter masses m_D and m_o using the following

$$p_D^2 - p_D rac{\mu^2 p_{v,||}}{E_v^2 - p_{v,||}^2} + rac{4E_v^2 m_D^2 - \mu^4}{4(E_v^2 - p_{v,||}^2)} = 0$$

where

$$\mu \equiv \sqrt{m_D^2 + m_v^2 - m_o^2}$$

The subscript v refers to the visible system, and the subscript || refers to the component of the momentum along the direction of flight of the parent.

There are in general two solutions to the above quadratic equation. Unphysical solutions are immediately rejected in our data, due to the fact that the visible mass m_{\bullet} is large in most cases. Futhermore we observe, and Monte Carlo studies confirm, that when there are two physical solutions for the momentum, the two solutions are always nearly equal to each other. Therefore in such cases the mean of the parent momentum given by the two solutions was used.

In nearly all of the decays for which constrained fits failed, one can find numerous 0C charm decay solutions. It is observed, and has been verified by Monte

Carlo studies, that for most decays the parent momentum calculated via the 0C assumptions is nearly independent of the charm species and the exact decay mode (only Cabibbo favored decays are attempted). The following are 0C solutions for a typical event taken from our data sample

Kinematic hypothesis	$x_{F,1}$	$x_{F,2}$	$p_{T,1}^2$	$p_{T,2}^2$
$D^+ o \pi^+ \pi^+ K^- \pi^o$	-0.034	-0.008	1.249	1.851
$D^+ o e^+ \pi^+ K^- u$	-0.036	-0.004	1.220	1.980
$D^+ o \pi^+ e^+ K^- u$	-0.036	-0.003	1.220	1.991
$D_s^+ o \pi^+\pi^+K^-K^o$	-0.021		1.589	

where $x_{F,1}$, $x_{F,2}$, $p_{T,1}$, and $p_{T,2}$ correspond to the two solutions of the quadratic equation in the parent momentum. Note the small variation of the x_F ($\Delta x < 0.1$) and p_T values.

As the 0C calculation can only be applied when all charged decay products were reconstructed, a method was developed to treat those cases where one charged track was outside the spectrometer acceptance. In this '0°C' calculation the missing charged track was grouped with the missing neutral into a system with an assumed invariant mass of $500 \text{ MeV}/c^2$ and the calculation proceeds identically to the 0C case.

In contrast to 0C results, the two solutions for the parent momentum from '0°C' calculations were often widely separated. However, as the geometric acceptance of the spectrometer was $\simeq 100\%$ for $x_F \geq 0$ (see Tables 1 and 2) the phase space

In other words if the parent had the high momentum of the fast solution, all charged decay products should have been reconstructable. The fast solution was therefore eliminated and a correction for the slow solution was calculated by Monte Carlo.

4.2.3 Graphical techniques

A program, E743PIX⁴, was written and used to improve our event reconstruction efficiency through graphical displays. Since the mean event multiplicity at our energy is $\simeq 10$, and each charm decay adds several charged tracks, charm events were topologically complex. Software tracking and kinematic fitting were performed by FLOWERS and GEO743. Events were then individually examined with E743PIX, a package for display and visual pattern recognition. Tracks that were not reconstructed in software were recovered in this phase by scanning the spectrometer hits, guided by the film measurements of decay track angles.

Spectrometer events were displayed in two views, the bend plane view x and the vertical plane view y. The y projections of decay tracks were found using roads defined by track angles as measured in the bubble chamber. The upstream x projections of these tracks were also found in that manner. Extrapolation of the upstream x roads to the mid magnet plane defined the intersection region for up and downstream legs in the bend plane. Downstream x projections were found by scanning wire chamber hits in that view. The graphics track candidates were subjected to the same selection

⁴A. Nguyen, E743 internal note

Table 4.1: Spectrometer acceptance as a function of x_F and topology (V2, C3, V4), requiring all charged decay tracks to be reconstructed.

x_F	V2	С3	V4
< -0.2	0.00	0.00	0.00
-0.20	0.02	0.00	0.00
-0.16	0.04	0.00	0.00
-0.12	0.11	0.00	0.00
-0.08	0.22	0.16	0.00
-0.04	0.46	0.43	0.34
0.00	0.75	0.67	0.59
0.04	0.92	0.85	0.75
0.08	0.95	0.90	0.87
0.12	0.96	0.97	0.92
0.16	0.97	0.98	0.98
0.20	0.99	1.00	0.99
> 0.2	1.00	1.00	1.00

Table 4.2: Spectrometer acceptance as a function of x_F and topology (V2, C3, V4), requiring at least two charged decay tracks to be reconstructed.

x_F	V2	С3	V4
< -0.2	0.00	0.00	0.00
-0.20	0.02	0.04	0.12
-0.16	0.04	0.14	0.31
-0.12	0.11	0.28	0.55
-0.08	0.22	0.61	0.83
-0.04	0.46	0.89	0.99
0.00	0.75	0.97	1.00
0.04	0.92	1.00	1.00
0.08	0.95	1.00	1.00
0.12	0.96	1.00	1.00
0.16	0.97	1.00	1.00
0.20	0.99	1.00	1.00
> 0.2	1.00	1.00	1.00

criteria as those found in software and submitted to GEO743 for further kinematic fitting.

In this and the previous chapter we have given detailed descriptions of our apparatus and our procedures for data reduction. The next chapter will deal with the study of our interaction trigger efficiency and the related topic of topological cross sections.

Chapter 5

NORMALIZATION AND MULTIPLICITY DISTRIBUTION

We describe in this chapter our procedures and results for the multiplicity distribution in proton-proton collisions at 800 GeV/c. This determination of the topological cross sections was crucial in our study of the interaction trigger bias. It is also worth mentioning that these are the only multiplicity data available at our energy.

5.1 Scaning of the data sample taken with an unbiased trigger

A total of 8.1×10^4 bubble chamber photographs were taken with an unbiased, 'beam' trigger. The trigger required only an incident beam track. Scanning of this film revealed 1.6×10^4 proton-proton interactions.

Beam arrived at varying times relative to the beginning of the bubble chamber expansion cycle. Events that were out of time had anomalous bubble size. To eliminate early and late events from the sample our scanners were equipped with templates of bubble sizes. Only events with bubbles in the range 20 μ m \leq bubble diameter \leq 100 μ m entered the sample. The final selected sample consisted of 11,828 events.

Table 5.1: Scanning efficiency for the multiplicity sample.

Multiplicity	Double scan efficiency
2	0.61 ± 0.07
4	0.92 ± 0.03
6	0.94 ± 0.03
8	0.99 ± 0.01
10	0.99 ± 0.01
≥ 12	1.00

Both views of each event were scanned. When an interaction was seen, the charge multiplicity was determined and recorded. A fraction of the sample was independently rescanned to measure the scanning efficiency. Scanning efficiency was dependent on the event multiplicity. Because there were fewer ionizing tracks the scanning efficiency was lower for events with low multiplicity (see Table 1).

The raw multiplicity distribution was corrected for scanning losses and for contamination by Dalitz decays of neutral pions. In two pronged events contamination by energetic knock on electrons (δ rays) and by elastic proton-proton scattering were evaluated and removed.

5.2 Determination of the multiplicity distribution

Our goal was to measure the primary multiplicity of inelastic proton-proton events. Decay tracks can be mistaken for primary tracks if their impact parameters were less than 100 μ m and the decay vertex was close to the primary vertex.

Pions and kaons were copiously produced but due to the relatively long lifetime of strange particles, the only appreciable background came from Dalitz decays of neutral pions, $\pi^o \to \gamma e^+e^-$, with branching fraction $BR(\frac{\pi^o \to \gamma e^+e^-}{\pi^o \to all}) = 1.2\%$.

Since there are two pion charged states and one neutral state with a small mixture of the η_8^o , isospin invariance dictates that the ratio of the production rates of charged to neutral pions should be approximately 2:1. Using the fact that roughly 90% of the fragments in hadron collisions are pions

$$< N(\pi^o) > \approx 0.45 < N_{ch} > .$$

Due to the short π° lifetime tracks from their Dalitz decays were not distinguishable from primary tracks and caused a 0.5% background in our multiplicity sample, i.e. \approx 60 obscured decays.

There was no magnetic field across LEBC and therefore δ rays (atomic electrons scattered by beam protons) cannot be unambiguously identified. Two pronged events therefore contained δ rays as well as inelastic and elastic contributions. A Monte Carlo simulation based on the expected kinetic energy distribution of δ rays, on their multiple scattering, and on their momentum to range relation gave a 6% δ ray contamination in the two pronged sample.

The total and elastic proton-proton cross section has been measured at surrounding energies¹. An interpolation between $\sqrt{s} = 30.7$ and 45.0 GeV gave

$$\sigma_{el} = 7.3 \pm 0.1 mb, \sigma_{tot} = 41.0 \pm 0.3 mb.$$

The number of inelastic two pronged events was calculated using

$$N_{2,inel} = N_{tot}(1 - \frac{\sigma_{el}}{\sigma_{tot}}) - N_{>2}$$

where N_{tot} is the corrected total number of events in the multiplicity sample, and $N_{>2}$ is the corrected number of events with more than two outgoing tracks. A total of 1,670 raw two pronged events were recorded. After corrections,

$$N_2 = 2758 \pm 183, N_{2,inel} = 510 \pm 191.$$

The topological cross sections were determined by normalizing to the above interpolated value for the total cross section. Table 2 summarizes our topological cross sections results and the multiplicity distribution is displayed in Figure 1.

Available data on charged particle multiplicity in inelastic proton-proton collisions have been fitted to the form²

$$< N_{ch} > = a + b \log(s) + c \log^2(s),$$

$$a = 0.800 \pm 0.120, b = 0.470 \pm 0.050, c = 0.114 \pm 0.005.$$

¹V. Flaminio et al., CERN-HERA 84-01 (1984)

²A. Breakstone et al., Phys. Rev. <u>D30</u> (1984) 528

Table 5.2: Observed topological cross sections.

Topology (N _{ch})	Raw number	Corrected number	Cross section (mb)	
2	1670	2758 ± 183	8.9 ± 0.6	
2(inelastic)	-	510 ± 191	1.6 ± 0.6	
4	1221	1238 ± 35	3.88 ± 0.11	
6	1478	1490 ± 39	4.67 ± 0.12	
8	1582	1590 ± 40	4.98 ± 0.12	
10	1535	1539 ± 39	4.82 ± 0.12	
12	1413	1404 ± 37	4.40 ± 0.12	
14	1094	1078 ± 33	3.38 ± 0.10	
16	747	734 ± 27	2.30 ± 0.07	
18	487	478 ± 22	1.50 ± 0.07	
20	232	312 ± 18	0.98 ± 0.06	
22	176	170 ± 13	0.53 ± 0.04	
24	102	97 ± 10	0.30 ± 0.03	
26	44	43 ± 7	0.13 ± 0.02	
28	29	27 ± 5	0.08 ± 0.02	
30	12	11 ± 3	0.03 ± 0.01	
32	6	6 ± 3	0.02 ± 0.01	
All	11828	12975 ± 209	$\textbf{(41.0 \pm 0.3)}$	

Figure 5.1: The multiplicity distribution.

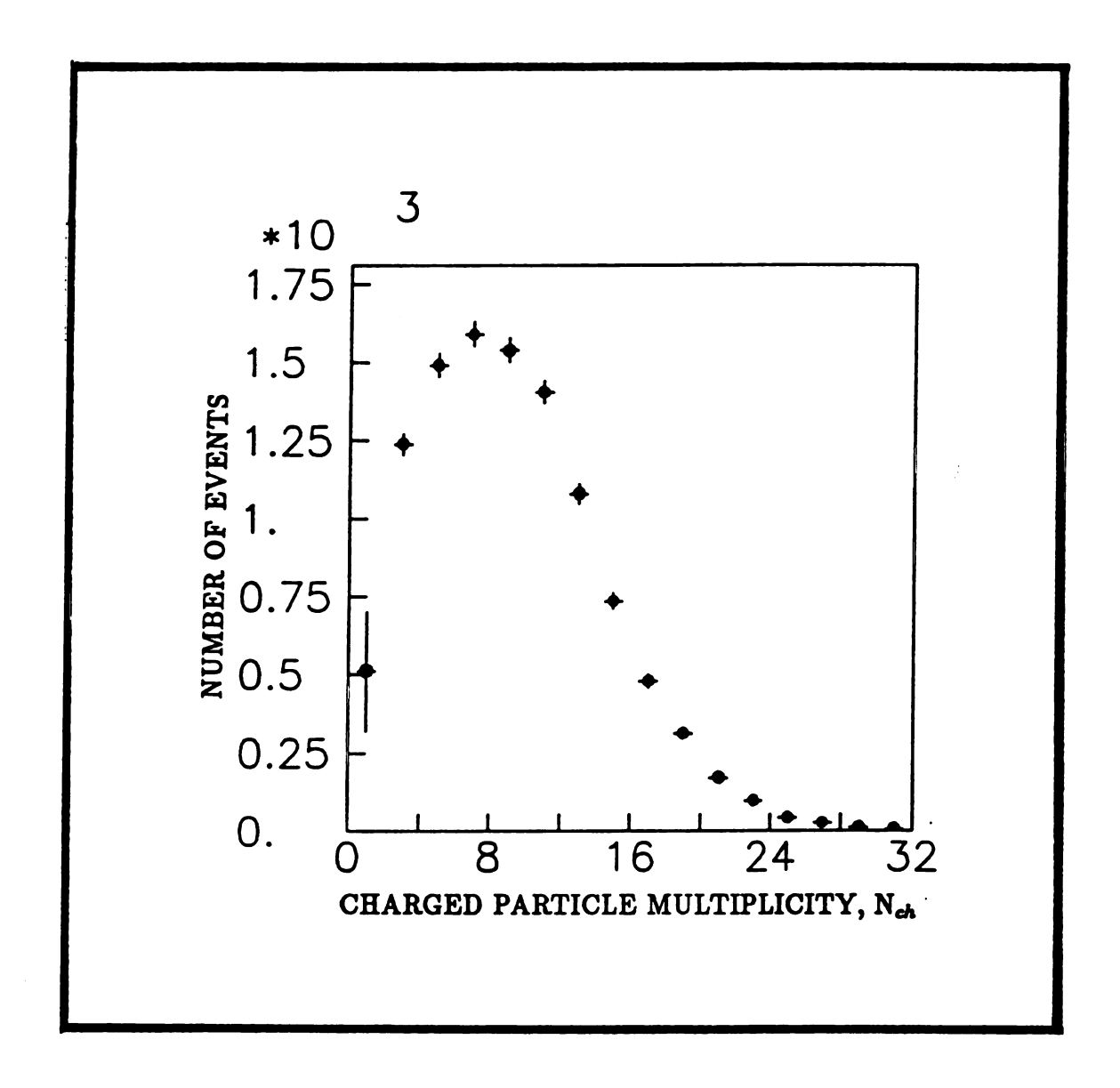


Table 5.3: Lowest moments of the observed inclusive multiplicity distribution.

Mean	$< N_{ch} >$	10.26 ± 0.15
Dispersion	D	5.19 ± 0.08
Skewness	$\frac{<(N_{ch}-< N_{ch}>)^3}{D^3}$	0.66 ± 0.03
Kurtosis	$\frac{<(N_{ch}-< N_{ch}>)^4}{D^4}$	3.27 ± 0.08
Second moment	$C_2 = \frac{\langle N_{ch}^2 \rangle}{\langle N_{ch} \rangle^2}$	1.26 ± 0.01
Third moment	$C_3 = \frac{\langle N_{ch}^3 \rangle}{\langle N_{ch} \rangle^3}$	1.85 ± 0.05
Fourth moment	$C_4 = \frac{\langle N_{ch}^4 \rangle}{\langle N_{ch} \rangle^4}$	3.09 ± 0.12

Figure 2 shows the energy dependence of $< N_{ch} >$. The mean charged multiplicity calculated from the above expression for $\sqrt{s} = 39$ GeV is 10.34 ± 0.15 , so that our value of $< N_{ch} > = 10.26 \pm 0.15$ is in good agreement with this parametrization.

Figure 3 shows the energy dependence of the lowest normalized multiplicity moments C_i , $1 \le i \le 5$. Our data yielded the results shown in Table 3. As can be seen, our values for the multiplicity moments smoothly interpolate measurements made by other experiments at surrounding energies.

Also of interest is the mean multiplicity for non-diffractive proton-proton events. If we assume that the dominant contributions to the two and four prong multiplicities are due to a diffractive mechanism, by removing those events with ≤ 4 prongs from the inclusive multiplicity distribution we obtain a mean multiplicity for an assumed

³G. J. Alner et al., CERN-EP/85-62 (1985)

Figure 5.2: The energy dependence of the mean charge multiplicity; the solid point is our measurement.

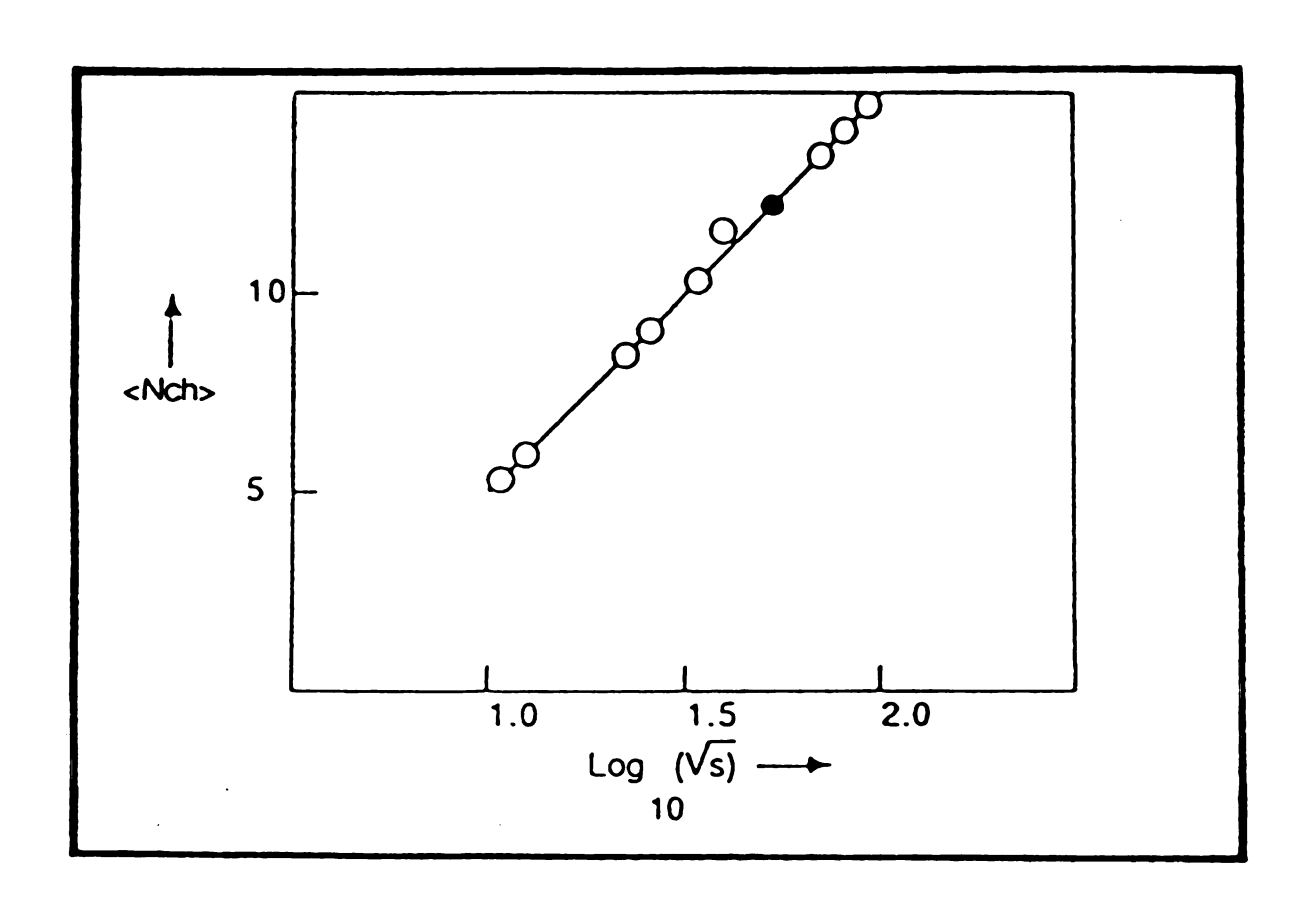
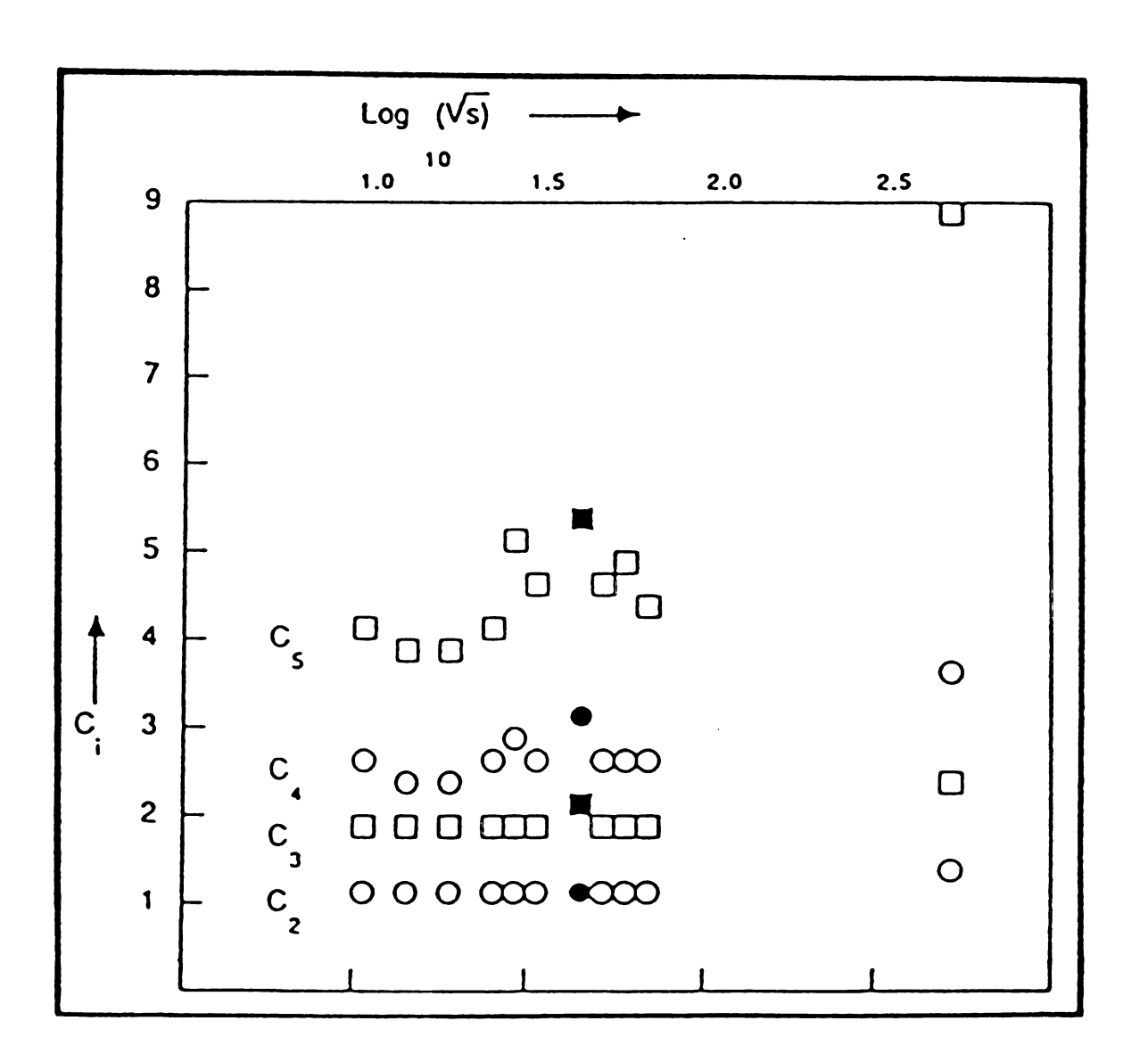


Figure 5.3: Energy dependence of the (normalized) higher multiplicity moments; the solid points are from our experiment.



non-diffractive mechanism of

$$< N_{ch,non-diffractive}> = 11.59 \pm 0.16, pp \rightarrow X \geq 6 prongs.$$

The topological cross section of two and four pronged events was ≈ 6 mb.

We have also measured the charge multiplicity in charm associated events. For charm events the mean primary multiplicity was

$$< N_{ch} > = 12.5 \pm 1.0, pp \rightarrow charm + X.$$

Charm decays with very short flight times were obscured by the high density of tracks near the production vertex. A Monte Carlo simulation developed by the author was used to evaluate contaminations of the primary multiplicity by tracks from such short lived charm particles. It was found that on average the charge multiplicity included 0.6 ± 0.2 tracks from obscured charm decays. Including this correction, the mean primary multiplicity in charm associated events became

$$< N_{ch} > \rightarrow 11.9 \pm 1.0.$$

5.3 Determination of the interaction trigger bias

The interaction trigger bias was determined by comparing the topological cross sections of 'beam' triggered events to those seen in 'interaction' triggered events. The two multiplicity distributions were normalized by requiring that the relative number of events with twelve or more prongs be the same for both distributions. The

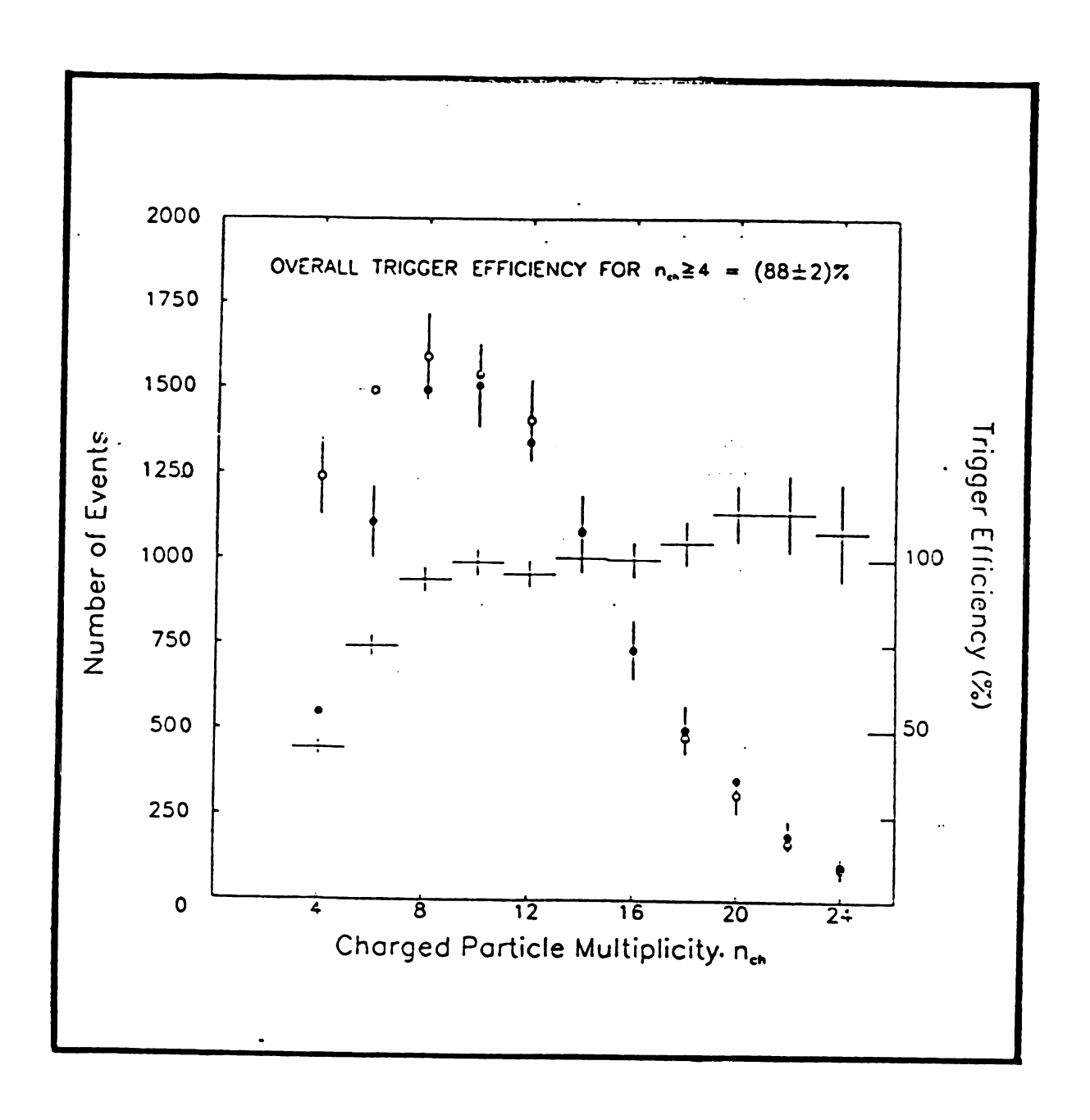
interaction trigger efficiency was taken as the ratio of the two distributions,

$$\epsilon(N_{ch}) = rac{P_{int}(N_{ch})}{P_{beam}(N_{ch})}.$$

Figure 4 shows the two normalized distributions as well as the interaction trigger efficiency. The interaction trigger was 50% efficient for four pronged events and rose to 100% for events with more than six prongs. The overall efficiency was $(88 \pm 2)\%$ for $N_{ch} \geq 4$. Since each charm decay adds several charged tracks, the efficiency was $\approx 99\%$ for charm associated events.

To summarize, we have described in this chapter our determination of the topological cross sections in inclusive proton-proton interactions. We have used that information to study the bias of the interaction trigger used to acquire our charm data sample. The next two chapters will deal directly with our results on charm hadroproduction. Chapter 6 describes the most important measurement made in E743, namely the cross section for D mesons, and Chapter 7 gives our results for their longitudinal and transverse momentum distributions.

Figure 5.4: Efficiency of our interaction trigger; solid points are the interaction triggered multiplicity distribution, open points are beam triggered; the curve is the interaction trigger efficiency.



Chapter 6

DETERMINATION OF THE CHARM INCLUSIVE CROSS SECTION

This chapter describes the most important measurement made in our experiment, the inclusive cross section for D mesons. The results reported here are derived from the first analyzed 25% of the bubble chamber film, corresponding to an experimental sensitivity of 3.5 \pm 0.1 events per μ b. Film scanning and measuring resulted in forty eight charm candidates, thirty four of which had the C3 topology and fourteen were V4's.

6.1 Normalization and systematic uncertainties

Charm decays have topologies C-odd or V-even. Because the C1 and V2 topologies were heavily contaminated by decays of strange particles, we only considered the C3 and V4 topologies in our cross section determination. By applying geometrical cuts, twenty five decays including twenty one C3's and four V4's were selected from the initial sample of forty eight charm candidates for the purpose of determining the D meson cross section.

The geometrical cuts imposed on the charm sample were designed to ensure clear definition of decay topologies, to minimize the number of D, and Λ_c decays in the D sample, and to remove the residual background of strange decays. The cuts were

- length cut: the decay length L must be at least 2 mm,
- angle cuts: no more than one decay track can have $\phi \geq 150$ milliradians (ϕ is approximately the angle between the track projection onto the film plane and the beam direction) and the angle between each pair of decay tracks must exceed 2 milliradians,
- maximum impact parameter cut: for C3's, 100 μ m $\leq Y_{max} \leq 2{,}000~\mu$ m and for V4's 50 μ m $\leq Y_{max} \leq 1{,}000~\mu$ m, and
- minimum impact parameter cut: $Y_{min} \ge 20 \ \mu \text{m}$.

Table 1 shows the statistics for our D meson sample, including the effects of the cuts.

The inclusive cross sections for D mesons were determined according to

$$\sigma(D^+/D^-) = \frac{N(C3) \times w(C3)}{s \times BR(C3) \times \epsilon},$$

$$\sigma(D^{o}/\overline{D}^{o}) = \frac{N(V4) \times w(V4)}{s \times BR(V4) \times \epsilon},$$

where

 $N \equiv$ the number of decays observed,

 $w \equiv$ a correction factor accounting for losses of events due to bubble chamber acceptance and to the geometrical cuts,

 $s \equiv$ the sensitivity (3.5 \pm 0.1 events per μ b),

 $BR \equiv$ the topological branching ratio, and

 $\epsilon \equiv$ the scanning efficiency (90 ± 5)%.

The correction factor w was determined for each topology by a Monte Carlo method (Appendix B) assuming

$$\frac{d^2\sigma}{dx_Fdp_T^2} \sim (1-|x_F|)^5 exp(-1\times p_T^2)$$

for D meson production, and phase space decay of the D's into dominant decay modes.

The weights were

$$w(C3) = 2.5 \pm 0.1, w(V4) = 4.0 \pm 0.2.$$

The difference in the weights for the two topologies is due chiefly to the difference in lifetime between the charged and neutral species.

The topological branching ratios were extracted from SPEAR results^{1,2}, $BR(C3) = 0.43 \pm 0.10$, $BR(V4) = 0.17 \pm 0.04$. Excluding the uncertainty introduced by the topological branching ratios, the systematic uncertainty in our measurement due to errors on the correction factor w, the experimental sensitivity, and the scanning efficiency was estimated at 7%. The topological branching ratios are known to 23%.

¹I. Perussi et al., Phys. Rev. Lett. 39 (1977) 1301

²R. H. Schindler et al., Phys. Rev. <u>D24</u> (1981) 78

Table 6.1: The D meson sample and effects of the geometrical cuts.

Topology	C3	V4
Total number of decays	34	14
Length cut	6	3
Angle cuts	4	1
Y _{mas} cut	1	2
Ymin cut	2	4
Total after cuts	21	4

6.2 Cross section results

Based on the first analyzed 25% of the charm sample, including twenty one C3 decays and four V4 decays, the inclusive D meson production cross sections for all x_F were

The errors quoted above are statistical. As previously discussed, systematic uncertainties were estimated at 7%, excluding contributions from the branching ratios which are known to 23%.

In the next chapter we will present results for the longitudinal and transverse momentum distributions for D mesons, from our analysis of the spectrometer information on topologically identified charm decays.

Chapter 7

D MESON DIFFERENTIAL CROSS SECTIONS

As pointed out in Chapter 2, the production characteristics of charm particles have been a matter of considerable controversy over the past few years. In this experiment we have made two independent measurements of the D meson differential cross sections in x_F and p_T^2 . The first measurement was based on an analysis of the decay length distributions observed in the bubble chamber. Although indirect, this technique enabled us to take advantage of the large bubble chamber acceptance. The second technique, based on the reconstruction of decay products in the spectrometer, provided a direct measurement of the D meson differential cross sections, although some charm decays seen in the bubble chamber were lost due to limited spectrometer acceptance. Results of these two independent measurements were consistent with each other.

7.1 Observations based on film measurement

The longitudinal and transverse decay length distributions of topologically tagged charm decays for the first analyzed 25% of the charm sample are shown in Figures 1 and 2. These distributions were used to obtain an indirect measurement of the production momentum spectra as follows.

Decay lengths are given by $L_{||}=\frac{p_{||}ct}{M},~L_{\perp}=\frac{p_{\perp}ct}{M},$ where t is the proper decay time. Assuming

$$\frac{d^2\sigma}{dx_Fdp_T^2} \sim (1-|x_F|)^n exp(-bp_\perp^2)$$

for charm production, the decay length probability distributions were

$$egin{split} rac{dP(L_{||};n)}{dL_{||}} &\sim \int_{-1 \leq x_F \leq 1} (1-|x_F|)^n exp(rac{-ML_{||}}{p_{||}c au}) rac{dp_{||}}{dx_F} dx_F, \ rac{dP(L_{\perp};b)}{dL_{\perp}} &\sim \int_{0 \leq p_{\perp}} exp(-bp_{\perp}^2) exp(rac{-ML_{\perp}}{p_{\perp}c au}) dp_{\perp}, \end{split}$$

where τ is the mean life.

The probability distributions were normalized according to

$$\int_{L_{min} < L < L_{max}} (\frac{dP}{dL}) dL = 1$$

where L_{min} was the minimum length cut and L_{mas} was the maximum decay length allowed by the finite size of the bubble chamber fiducial volume. Since production vertices were uniformly distributed throughout the fiducial volume, each observed decay was assigned a weight

$$w_i = [exp(rac{-L_{min}}{\overline{L}}) - exp(rac{-L_{max}}{\overline{L}})]^{-1},$$

where the mean decay length \overline{L} was directly related to the lifetime of the particle for a given production n.

Maximum likelihood fits were performed to find the production parameters n and b. The likelihood functions were

$$\log[\mathcal{L}(n; L_{||})] = \Sigma_i \log[w_i P_i(L_{||})],$$

$$\log[\mathcal{L}(b; L_{\perp})] = \Sigma_i \log[w_i P_i(L_{\perp})],$$

where the sum extended over all observed decays. Maximization of the likelihood function with respect to the parameter of interest gives the best fit value for that parameter, while the standard (1σ) deviation is given by $\Delta n = |n_0 - n_1|$ where n_0 is the best fit value and n_1 is the value for which $\frac{\mathcal{L}(n_0)}{\mathcal{L}(n_1)} = \exp(1/2)$ (similarly for the parameter b). Fitting the observed transverse decay length distribution (see Figure 4) gave

$$b = 0.6^{+0.6}_{-0.4} (GeV/c)^{-2}$$
.

Because $-\log[\mathcal{L}(n;L_{||})]$ had a shallow minimum (see Figure 3), fitting the observed longitudinal decay length distribution did not give a precise measurement of the parameter n; the function minimized at $n \simeq 10$ and the 2σ error excluded $n \leq 4$.

7.2 Observations based on spectrometer information

Precise measurements of charm production parameters required momentum measurement of the products of topologically identified charm decays. Charm associated events were tagged in the bubble chamber. Complete tracking and hybridization was

Figure 7.1: The longitudinal decay length distribution.

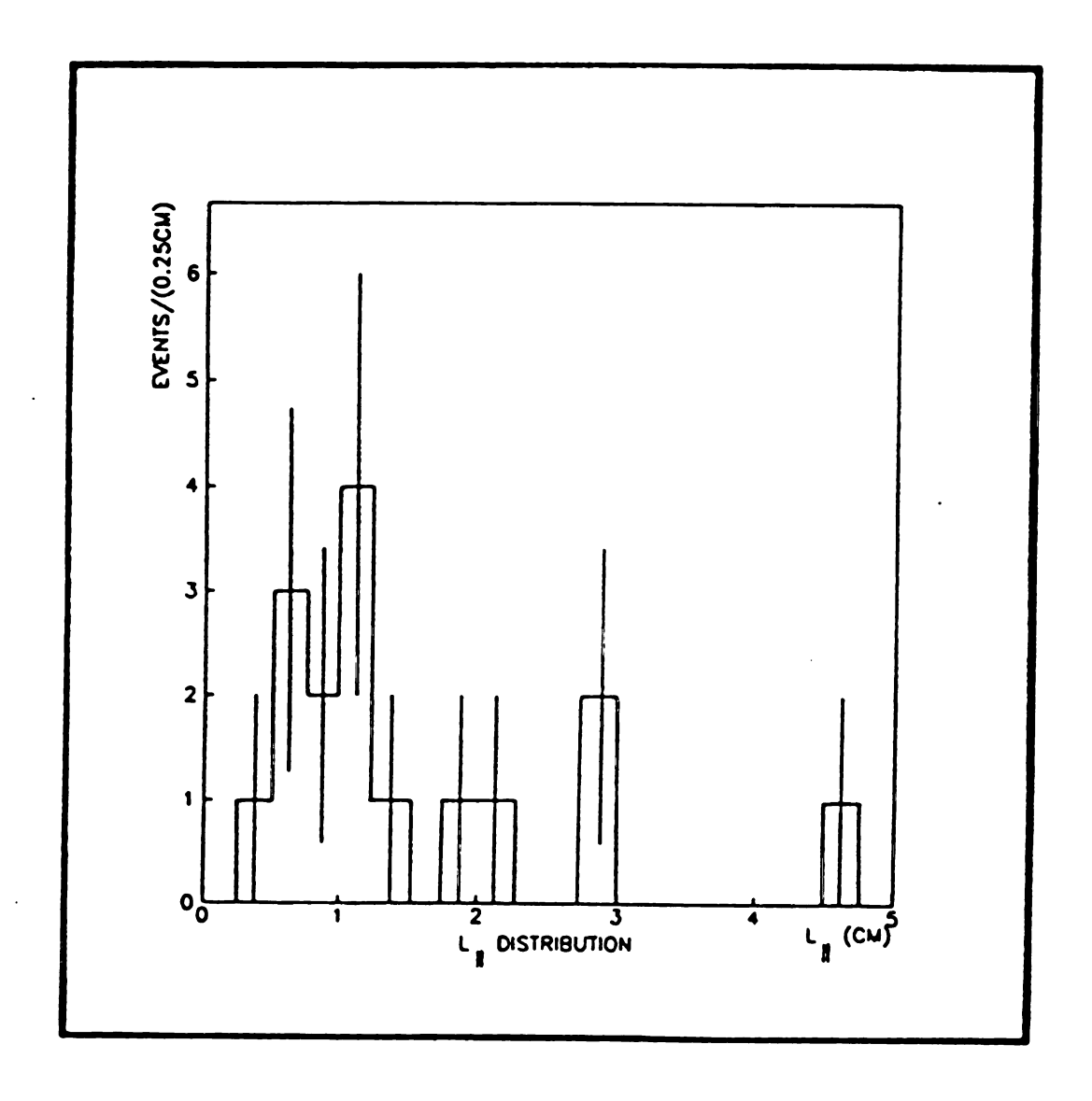


Figure 7.2: The transverse decay length distribution.

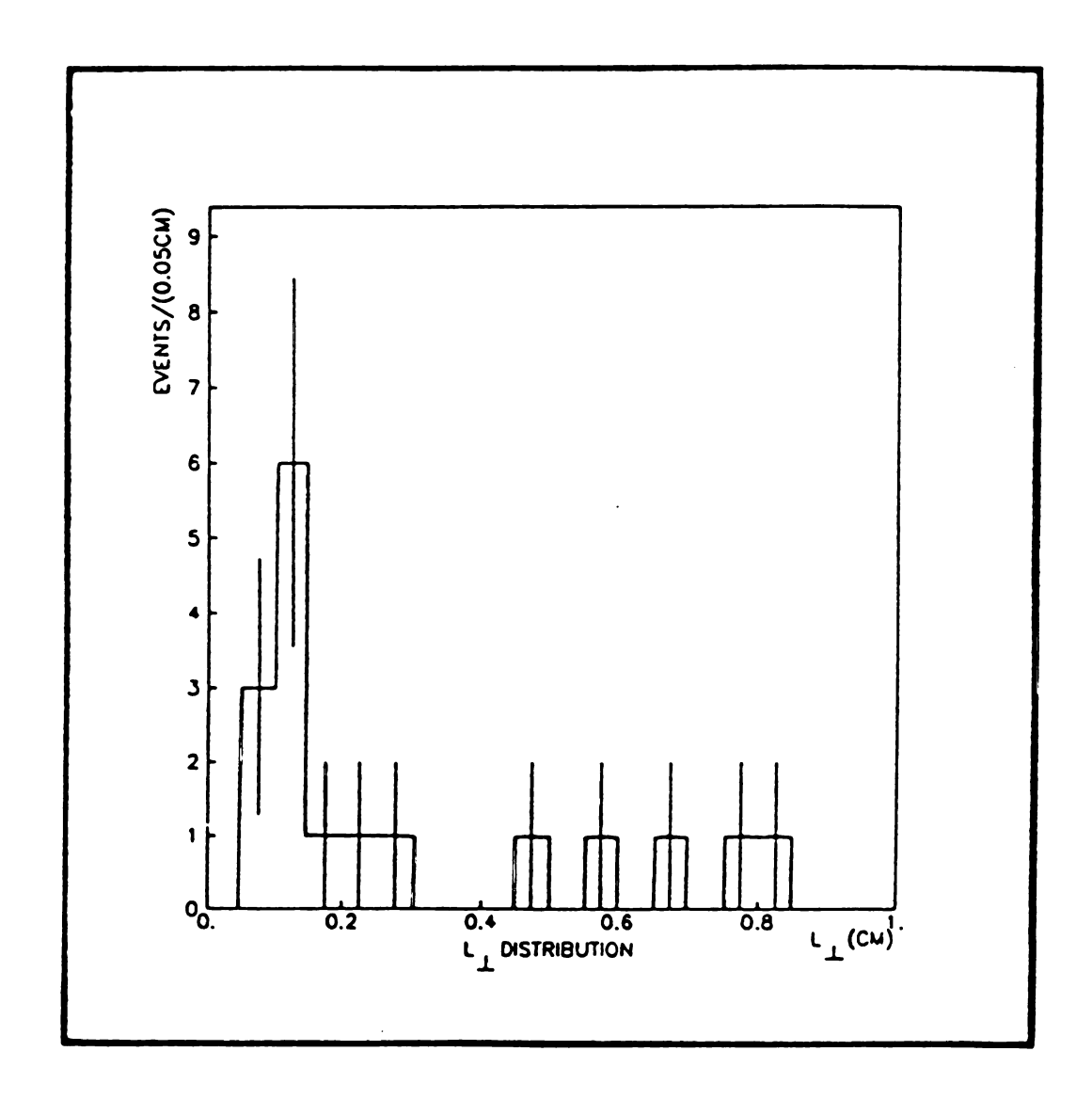


Figure 7.3: Maximum likelihood fit of the longitudinal decay length distribution.

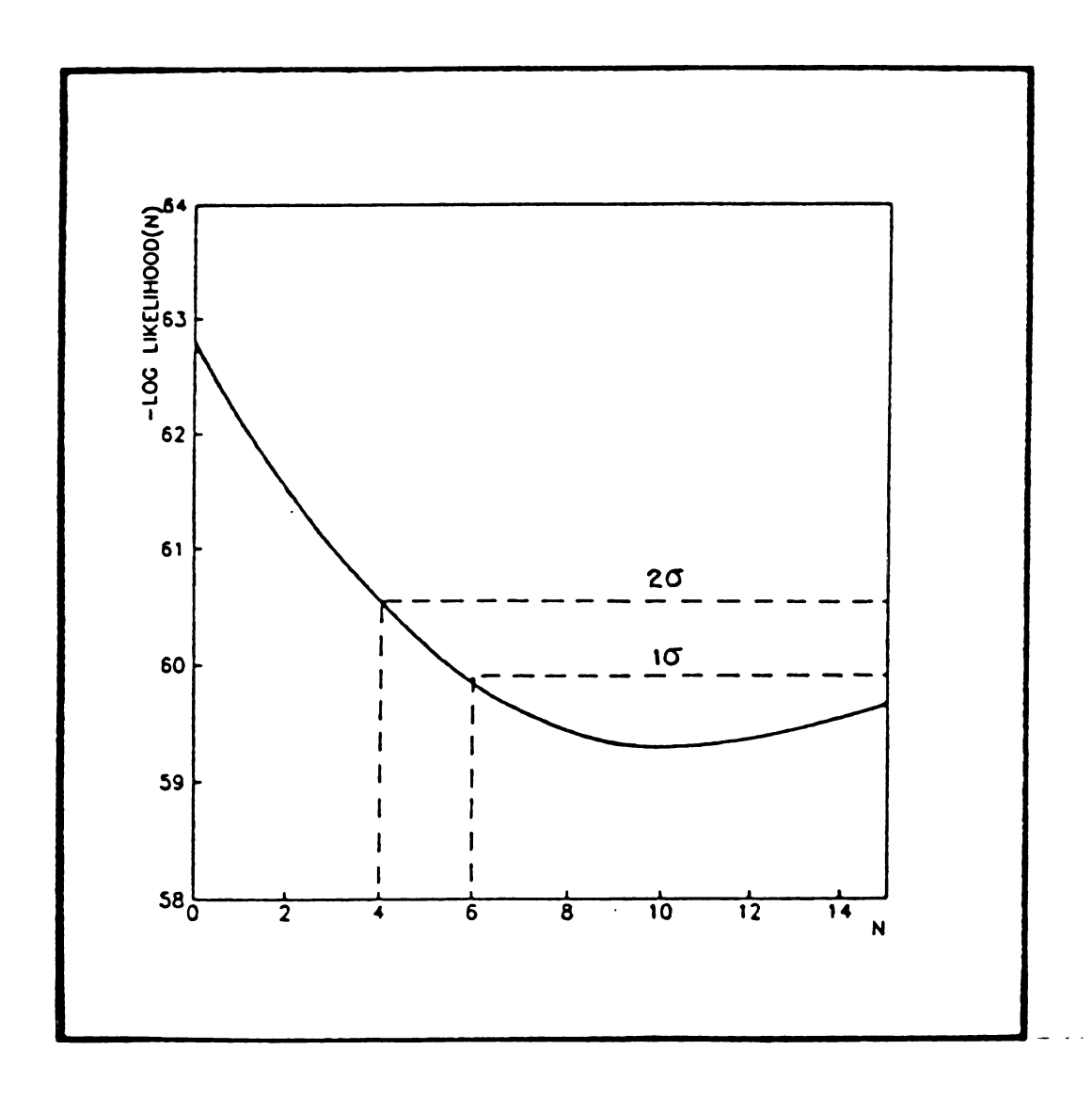
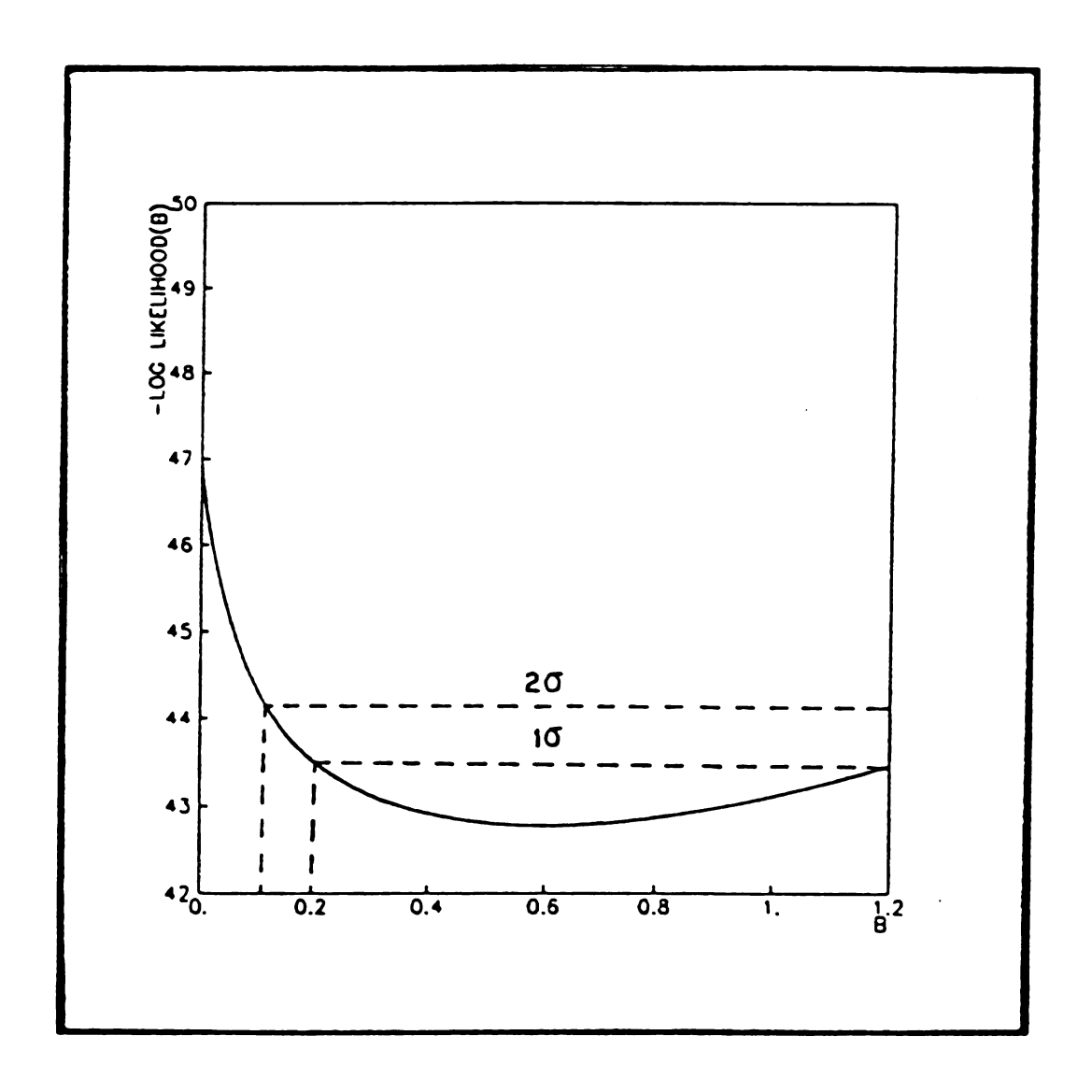


Figure 7.4: Maximum likelihood fit of the transverse decay length distribution.



performed for the event and kinematic fits of the decay products were carried out to determine the mass and momentum of the parent particle.

Reconstructed charm decays were assigned individual weights to correct for spectrometer and bubble chamber acceptance. Maximum likelihood fits of the weighted distributions were used to determine the production parameters n and b.

Kinematic fits of decays were categorized by constraint class. Only fits with at least two constraints (3C and 2C fits) were accepted. When all charged decay products were momentum analyzed but no constrained fits were found, indicating that one of the decay products was neutral, unconstrained (0C) calculations were used to obtain the momentum of the parent. In cases where no constrained fits were found and one charged decay product was outside the spectrometer acceptance, an extension of the 0C calculation ('0*C') was used to calculate the parent momentum.

Each decay was assigned a spectrometer weight and a bubble chamber weight, according to its topology and x_F . The spectrometer acceptance was $\simeq 100\%$ for positive x_F , the acceptance depended slightly on the topology. The spectrometer weight w_{spc} was calculated according to

$$w_{spc} = \frac{1}{\epsilon}$$

where ϵ is the spectrometer acceptance.

Given the momentum of the decaying particle, the bubble chamber visibility weight w_{vis} was calculated according to

$$w_{vis} = [exp(rac{-L_{min}}{\overline{L}}) - exp(rac{-L_{max}}{\overline{L}})]^{-1}$$

where L_{min} is the minimum detectable length, L_{max} is the maximum decay length, and \overline{L} the mean decay length uniquely determined by the lifetime and measured momentum of the parent particle.

The minimum detectable length L_{min} was that for which the minimum impact parameter of the decay exceeded 10 μ m and the maximum impact parameter exceeded 50 μ m. The length L_{max} was the maximum attainable before the decay vertex either went out of focus or out of the fiducial volume.

The sample under consideration consisted of forty four events from the first quarter of our film and included twenty one V2 decays, thirty one C3 decays, nine V4 decays, and three C5 decays. Eliminating decays with K^o , D_s , and Λ_c fits left twenty seven reconstructed D meson decays, including one 3C fit, five 2C fits, seven 0C solutions, and seven 0°C solutions (see Chapter 4 for the definition of these fitting classes). Fitted momenta are listed in Table 1.

Using the method of maximum likelihood, the corrected x_F distribution was fitted to the forms

$$rac{dN}{dx_F} \sim (1-|x_F|)^n, Erac{dN}{dx_F} \sim (1-|x_F|)^{n'}$$

(E is the energy of the charm particle), and the corrected p_T distribution was fitted to the form

$$rac{dN}{dp_T^2} \sim exp(-bp_T^2),$$

to determine the production parameters n, n', and b.

Table 7.1: Reconstructed D meson decays.

Topology	Fit	x_F	p _T	W_{vis}	W_{spc}
V4	3C	-0.03	0.41	1.80	1.01
C3	2C	0.07	0.75	1.28	1.00
C3	2C	0.07	1.39	1.10	1.00
С3	2C	0.01	1.34	1.08	1.03
V4	2C	0.25	1.68	1.40	1.00
V4	2C	0.13	0.82	1.26	1.00
V2	0C	-0.05	2.41	1.43	2.53
С3	0C	0.09	2.03	1.18	1.00
С3	0C	-0.02	1.53	1.19	1.08
С3	0C	0.00	0.81	1.15	1.03
СЗ	0C	0.09	0.86	1.34	1.00
СЗ	0C	0.02	0.14	1.39	1.00
V4	0C	-0.00	0.44	1.68	1.00
С3	0*C	-0.11	0.89	1.09	2.70
С3	0*C	0.01	4.64	1.35	1.03
С3	0*C	-0.14	0.45	10.41	4.68
V4	0*C	-0.02	1.34	2.07	1.01
V4	0*C	0.04	0.24	1.86	1.00
V4	0*C	0.01	0.65	1.96	1.00
C5	0*C	0.14	0.85	1.33	1.00

7.3 Differential cross section results

Figures 5 through 7 show the longitudinal and transverse momentum distributions for reconstructed D meson decays with $-0.1 \le x_F \le 1.0$ and $0 \le p_T \le 2.5$ GeV/c. Two decays, a V2 and a C3 with $x_F \approx -0.1$ occured in regions of poor spectrometer acceptance and therefore had relatively high weights. They were excluded from the fitted sample (fit results were insensitive to their exclusion). One C3 decay with $p_T = 4.6$ GeV/c was also excluded since the probability for that event is very small (< 10^{-6}). The D meson x_F and p_T distributions were well described by the parametrization

$$egin{split} rac{dN}{dx_F} &\sim (1-|x_F|)^n, n=11.0^{+4.6}_{-3.6}; \ &Erac{dN}{dx_F} &\sim (1-|x_F|)^{n'}, n'=7.8^{+4.5}_{-3.5}; \ &rac{dN}{dp_T^2} &\sim exp(-bp_T^2), b=0.66^{+0.23}_{-0.20}(Gev/c)^{-2}. \end{split}$$

Errors quoted are based on the 1σ values found by examination of the likelihood functions. These results for the parameters n and b consistent with those obtained from our analysis of decay length distributions. In addition, we observe no events at $|x_F| > 0.3$, which corresponds to an upper limit of 10 μ b at a 95% confidence level for D production at large x_F .

In the next chapter we will present a comparison of our results for the D meson total and differential cross sections to measurements made by other experiments at different energies, as well as to predictions made by various theoretical models for hadronic charm production.

Figure 7.5: The Feynman x distribution $\frac{dN}{dx_F}$.

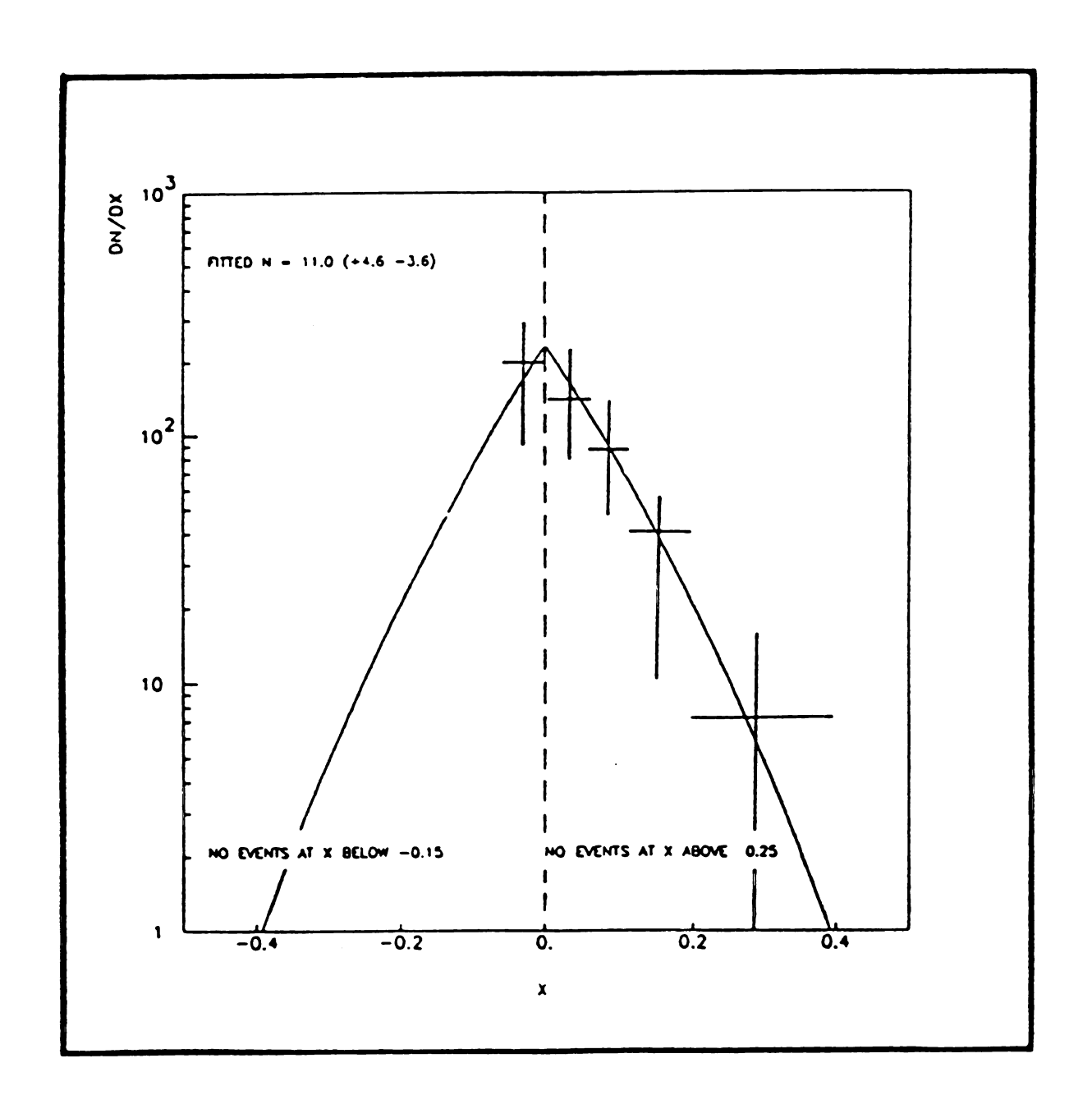


Figure 7.6: The invariant distribution $E\frac{dN}{dx_F}$.

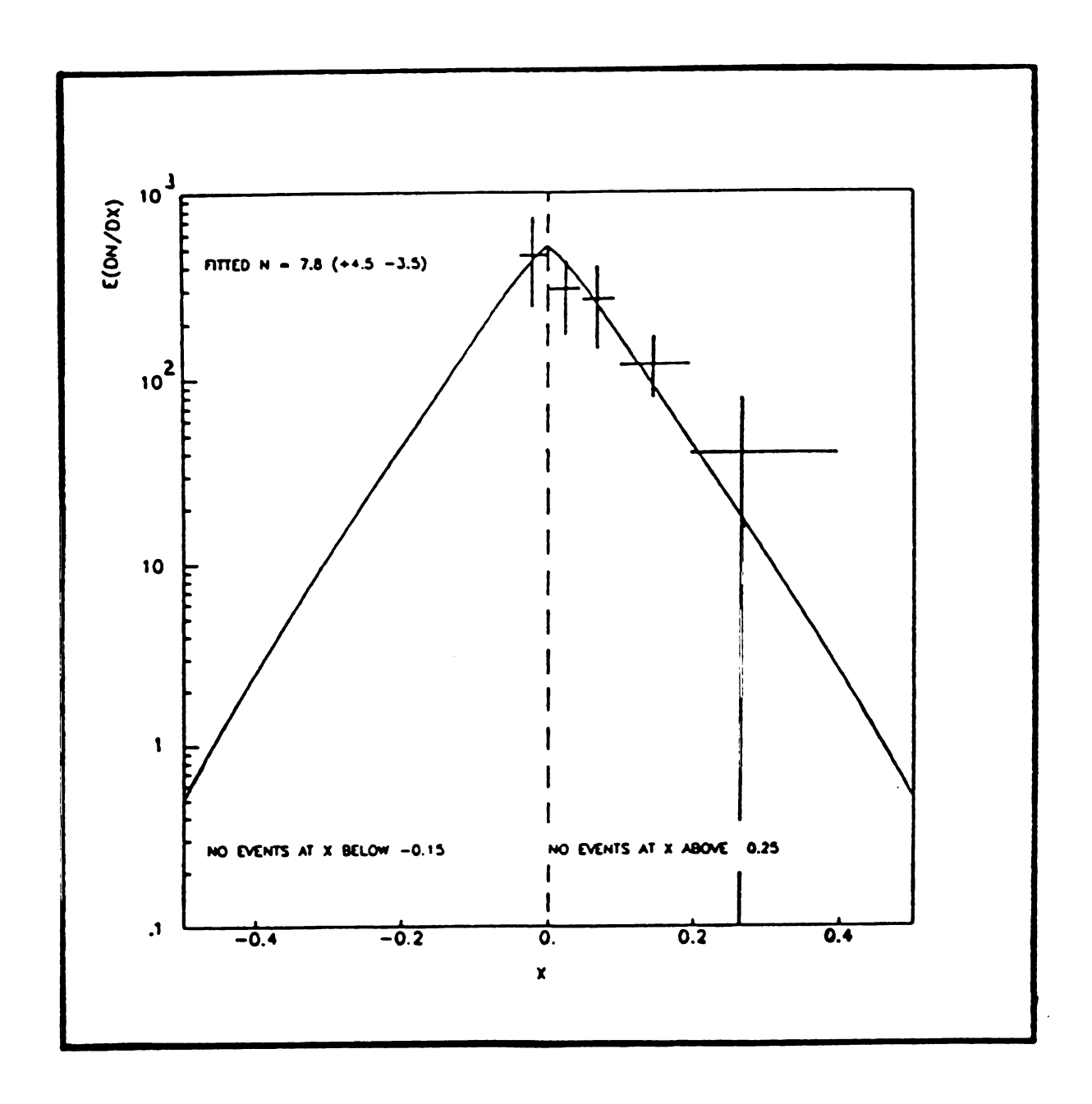
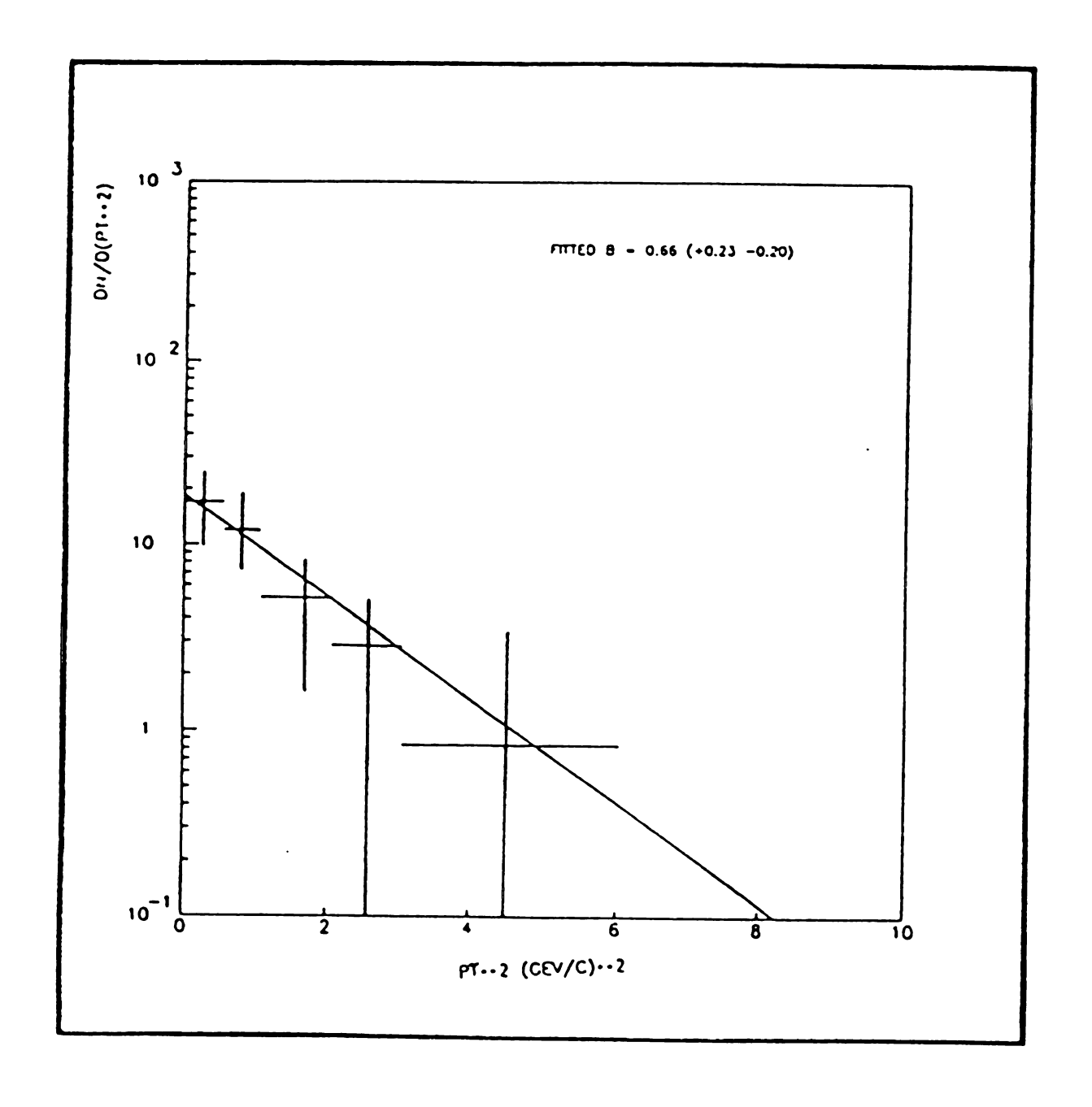


Figure 7.7: The transverse momentum distribution $\frac{dN}{dp_T^2}$.



Chapter 8

COMPARISON OF RESULTS WITH THE FUSION MODEL AND OTHER MECHANISMS

8.1 The experimentally observed energy dependence of the charm cross sections

We have seen that from a sample of twenty five observed D meson decays the inclusive production cross section for D mesons in proton-proton collisions is

$$\sigma(D/\overline{D}) = 59^{+22}_{-15}\mu b$$

 $(\sigma(D^+/D^-)=33\pm7\mu\mathrm{b},\ \sigma(D^o/\overline{D}^o)=26^{+21}_{-13}\mu\mathrm{b}),\ \mathrm{where\ the\ errors\ are\ statistical}.$ Systematic uncertainties were estimated at 7%, excluding the uncertainties introduced through branching ratios^{1,2}, which were known to 23%.

We have also measured the associated charged multiplicity in both charm and non-charm events. For charm events the mean primary multiplicity was

¹I. Perussi et al., Phys. Rev. Lett. <u>39</u> (1977) 1301

²R. H. Schindler et al., Phys. Rev. <u>D24</u> (1981) 78

 $< N_{ch} > = 11.9 \pm 1.0, pp \rightarrow {\rm charm} + {\rm X}, {\rm while} {\rm for inclusive proton-proton events}$ $< N_{ch} > = 10.26 \pm 0.15 (pp \rightarrow {\rm X}). {\rm Removing the diffractive component} (\sim 6 {\rm mb}) {\rm from}$ the inclusive multiplicity distribution yielded a non-diffractive mean multiplicity of $< N_{ch,non-diffractive} > = 11.59 \pm 0.16 (pp \rightarrow {\rm X} \ge 6 {\rm prongs}) {\rm which} {\rm is rather close to that}$ observed for charm associated events.

Experiment NA27 by the LEBC-EHS collaboration at the CERN SPS, using an identical version of our bubble chamber coupled to the European Hybrid Spectrometer, presented the following result³

$$\sigma(D/\overline{D}) = 34.4 \pm 4.2 \mu b$$

 $(\sigma(D^+/D^-) = 12.5 \pm 1.4 \mu b, \ \sigma(D^o/\overline{D}^o) = 21.9 \pm 4.0 \mu b), \ at center of mass energy$ $\sqrt{s} = 27 \text{ GeV}$ (an earlier measurement by experiment NA16⁴, also at the SPS but at $\sqrt{s} = 26 \text{ GeV}$, gave $\sigma(D^+/D^-) = 10.6^{+4.8}_{-3.2} \mu b, \ \sigma(D^o/\overline{D}^o) = 20.4^{+15.8}_{-8.6} \mu b).$

Experiments at the CERN ISR (53 GeV $\leq \sqrt{s} \leq$ 63GeV) reported very large charm cross sections⁵. Measurements of the D meson cross section at the Split Field Magnet gave values between 0.2 and 5.0 mb, with a flat x_F distribution. The determination of the cross section in these experiments depended critically on estimates of the acceptance of charm decay products in the apparatus, and on branching ratios into exclusive decay channels. A linear interpolation between the NA27 measurement

^{*}LEBC-EHS Collaboration, Berkeley Conf. Preprint, presented by M. E. Michalon and M. Iori

⁴M. Aguilar-Benites et al., Phys. Lett. <u>135B</u> (1984) 237

⁵S. L. Olsen, AIP Conference Proceedings No. 85 (1981) 1

and the ISR values would predict a dramatic growth of the cross section

$$rac{\sigma_{D\overline{D}}(\sqrt{s}=39GeV)}{\sigma_{D\overline{D}}(\sqrt{s}=27GeV)}pprox 10$$

over the small energy range from $\sqrt{s} = 27$ GeV to 39 GeV.

In contrast, taken together with the NA27 results our measurement of the D meson cross sections gives an energy dependence of

$$rac{\sigma_{D\overline{D}}(\sqrt{s}=38GeV)}{\sigma_{D\overline{D}}(\sqrt{s}=27GeV)}=1.7^{+0.6}_{-0.5}$$

Our analysis of the spectrometer information showed that the longitudinal momentum distribution of produced D mesons is well fitted by the parametrization

$$\frac{dN}{dx_F} \sim (1 - |x_F|)^n, n = 11.0^{+4.6}_{-3.6}$$

and that the transverse momentum distribution is well fitted by

$$rac{dN}{dp_T^2} \sim exp(-bp_T^2), b = 0.66^{+0.23}_{-0.20} (GeV/c)^{-2}$$

(the LEBC-EHS collaboration also fitted their observed differential cross sections to the above forms and reported $n=4.8\pm0.7,\,b=1.21\pm0.14(GeV/c)^{-2}$).

These results show that the charm hadroproduction cross section is increasing relatively slowly with center of mass energy, and that charm production occurs predominantly in the central x_F region. In addition, when compared to the NA27 measurements, our results indicate that the x_F distribution becomes more central with increasing energy.

8.2 Predictions by the Fusion model and by other mechanisms

A generally accepted model for hadronic production of charm, the Fusion model (FM), can reproduce most aspects of our data. As discussed in Chapter 2, the FM makes use of perturbative QCD and a phenomenological picture of the proton structure as well as the hadronization of quarks to predict charm cross sections and their energy dependence. Prediction of the absolute cross section is sensitive to input parameters such as the mass of the charm quark and the QCD scale parameter Λ , as well as to the parametrization used for the quark and gluon structure functions. Since the structure functions are evaluated at $Q^2 = 4m_c^2$, variations in the charm quark mass translate into changes in the longitudinal momentum fraction of the quarks and gluons in the collision.

Figure 1 shows recent FM predictions⁶ for the total hadronic charm production cross section, assuming extreme values 1.2 GeV/c² $\leq m_c \leq$ 1.8 GeV/c² for the charm quark mass (the parametrization by Duke and Owens⁷ was used with $\Lambda=200$ MeV for the QCD scale parameter). These predictions refer to the cross section for producing either a charm quark or antiquark (not summed); as no experimental evidence exists for correlations between the pair produced charm hadrons, and as the major contribution to the hadronic charm production cross section at our energy consists of

⁶R. K. Ellis and C. Quigg, Fermilab FN-445 (1987)

⁷D. W. Duke and J. F. Owens, Phys. Rev. D30 (1984) 49

D mesons, the FM would predict

$$\sigma_{FM}(D/\overline{D}) \simeq 40 \mu b, m_c = 1.2 GeV/c^2,$$

at $\sqrt{s}=39$ GeV $(\sigma_{FM}(D/\overline{D})\simeq 6\mu b, m_c=1.8$ GeV/c²). This prediction is smaller than our observed cross section by a factor K, K $\simeq 1.5$ for $m_c=1.2$ GeV/c² (K $\simeq 10$ for $m_c=1.8$ GeV/c²). K factors on the order of 2 are not unexpected in calculations where only first order QCD diagrams are included.

The FM prediction for the energy dependence of the charm cross section is not expected to be affected by the neglect of contributions from higher order diagrams.

An energy dependence of

$$\frac{\sigma_{FM}(\sqrt{s}=39GeV)}{\sigma_{FM}(\sqrt{s}=27GeV)} \simeq 2, m_c = 1.2GeV/c^2, (\simeq 3, m_c = 1.8GeV/c^2)$$

was predicted for charm production in proton-nucleon collisions. Our measurement of the inclusive D meson cross section favors light charm quark masses.

In addition, the FM predicted predominantly central production of D mesons in hadron collisions and, with reasonable assumptions for the mean intrinsic transverse momentum $\langle k_T \rangle$ of the constituents of the proton, the experimentally observed transverse momentum distributions were reproducible. Figures 2 and 3 show the predictions by Ellis and Quigg, superposed on our observed D meson Feynman x and transverse momentum distributions.

The Excitation model (EM) was proposed as an additional contribution to charm hadroproduction as an explanation for the dramatic rise in the charm cross section and the forward charm x_F distribution inferred from ISR measurements. Sim-

Figure 8.1: Fusion model predictions of the integrated charm hadronic production cross section.

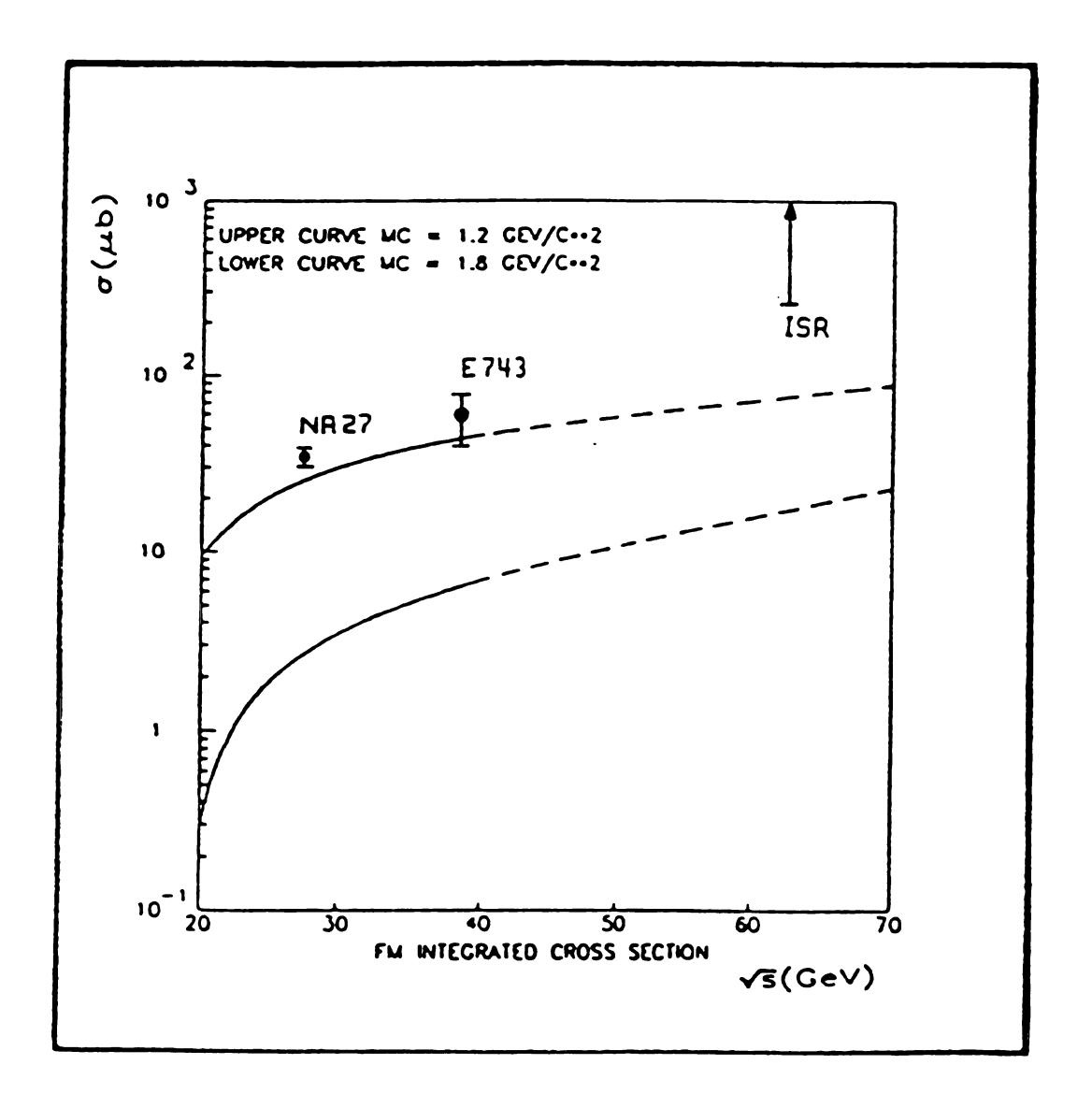


Figure 8.2: Fusion model predictions of the differential charm hadronic production cross section $\frac{dN}{dx_F}$: data points are from our experiment.

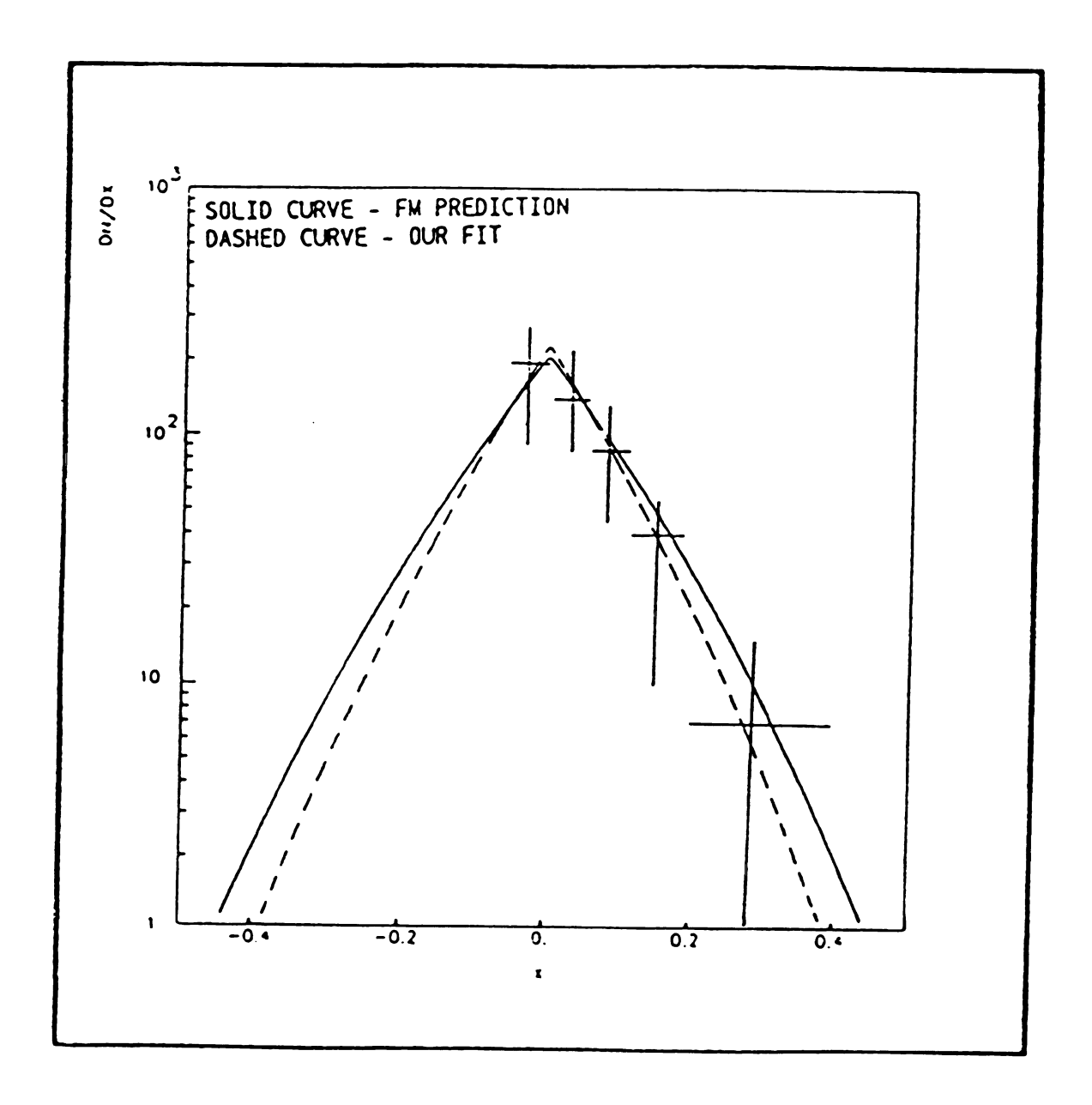
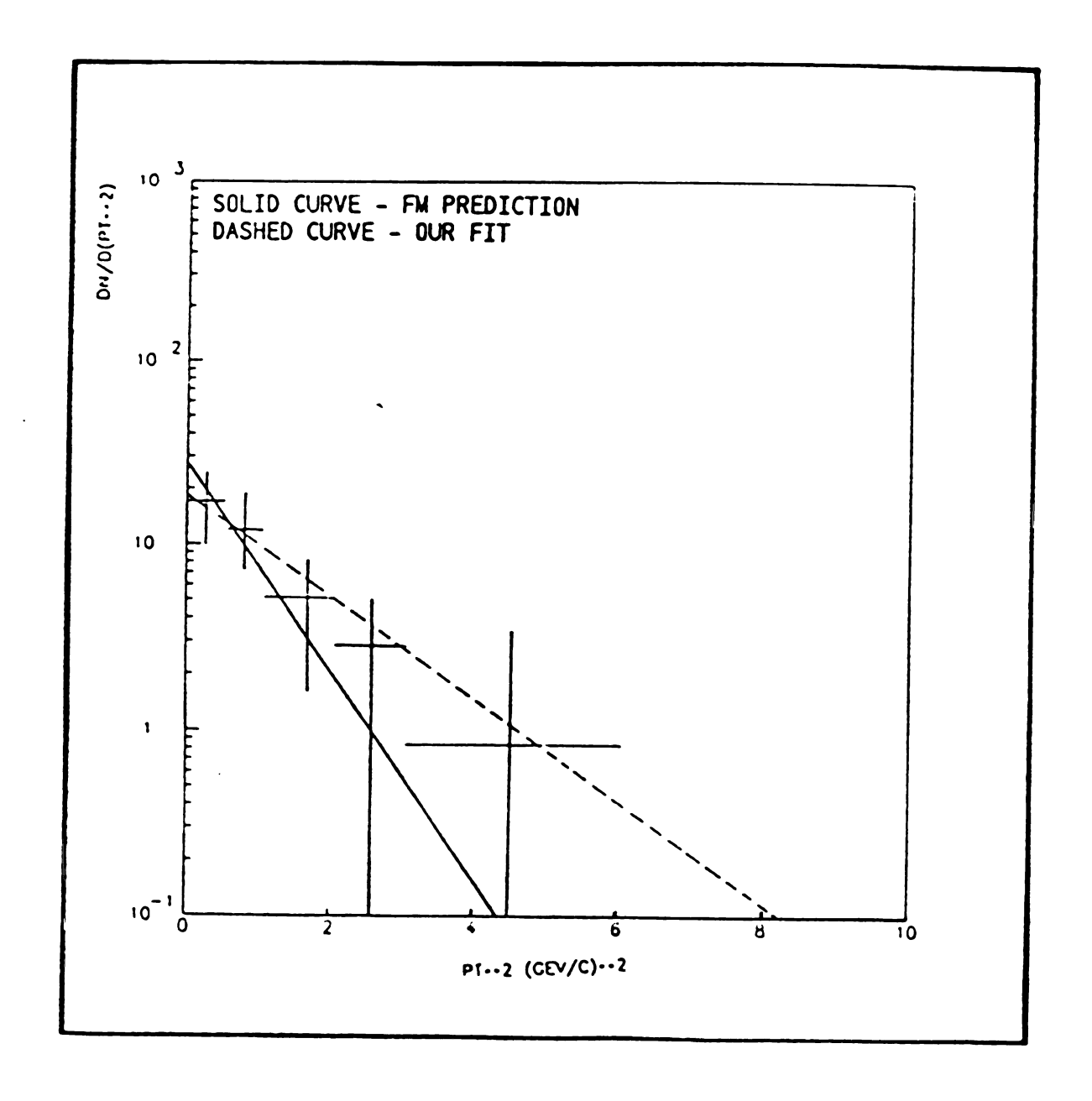


Figure 8.3: Fusion model predictions of the differential charm hadronic production cross section $\frac{dN}{dp_T^2}$: data points are from our experiment.



ilarly to the FM, the EM was a perturbative QCD treatment of hard scattering processes between hadron constituents. In the EM, a charm quark from the target sea hadronizes into a physical charm particle after colliding with a quark or gluon from the beam. As no measurement has been made of the charm sea distribution, this distribution was evolved from zero at low momentum transfers.

The EM calculations for the charm cross section were strongly dependent on the sea charm structure function and EM predictions had correspondingly large uncertainties. An early calculation gave⁸ $\sigma_{EM} \approx 10 \times \sigma_{FM}$, while later estimates⁹ gave $\sigma_{EM} \approx 2 \times \sigma_{FM}$, at $\sqrt{s} = 39$ GeV.

As both the FM and the EM are hard scattering mechanisms, these two models predict similar energy dependence for the cross section. However the EM longitudinal momentum distribution of charm hadrons is significantly different from FM predictions. The struck (excited) charm quark hadronizes by recombining with quarks from the sea and the Feynman x distribution of hadrons originating from struck charm quarks should be central. In addition, a large forward component is expected from hadrons originating from the spectator charm quarks since they recombine with valence quarks from the beam or target¹⁰.

Our measured D meson cross section is lower than the FM prediction by a factor of between 1.5 and 10 for various charm quark mass choices, thus some room for an

⁸B. L. Combridge, Nucl. Phys. <u>B151</u> (1979) 429

V. Barger, F. Halsen, and W. Y. Keung, Madison preprint DOE-ER/00881-215 (1981)

¹⁰R. Odorico, AIP Conference Proceedings No. 85 (1981) 100

EM contribution to charm hadronic production at $\sqrt{s} = 39$ GeV is available. However, our observation of predominantly central D meson production contradicts the expectations of the EM for forward production of D mesons via specific recombination mechanisms.

The Intrinsic charm model (ICM) was proposed as an alternative to hard scattering mechanisms, to explain forward charm production with large cross sections¹¹ observed at the ISR. The ICM postulates a non negligible $uudc\bar{c}$ component of the proton wavefunction. Due to the large mass of the charm quark the intrinsic $c\bar{c}$ pair carries a large fraction of the proton momentum and at high energies only a small momentum transfer is required to excite an intrinsic charm quark into a fast moving charm hadron in diffractive scattering.

The charm total cross section was expected to be large and to come almost entirely from diffraction, $\sigma_{ICM} \approx 500 \mu b$ at $\sqrt{s} = 63$ GeV. A linear interpolation between the above prediction and the NA27 measurement at $\sqrt{s} = 27$ GeV would predict a large charm cross section at our energy, $\sigma_{ICM}(\sqrt{s} = 39 GeV) \sim 200 \mu b$ corresponding to a rise in the cross section of

$$\frac{\sigma_{ICM}(\sqrt{s}=39GeV)}{\sigma_{ICM}(\sqrt{s}=27GeV)}\sim 10$$

with increasing center of mass energy.

The ICM values are inconsistent not only with the observed energy dependence of charm production but also with the predominantly central longitudinal momentum

¹¹S. J. Brodsky, P. Hoyer, C. Peterson, and N. Sakai, Phys. Lett. <u>93B</u> (1980) 451

distribution of D mesons in our study.

Chapter 9

CONCLUSIONS

We have presented in this thesis the results of Fermilab experiment E743 on hadronic production of D mesons. By directly observing charm decay vertices in the high resolution, rapid cycling hydrogen bubble chamber LEBC and by reconstructing charm associated events in the MPS spectrometer, we have made a relatively unbiased measurement of the inclusive D meson cross section in 800 GeV proton-proton collisions,

$$\sigma(D/\overline{D}) = 59^{+22}_{-15}\mu b$$

$$(\sigma(D^+/D^-) = 33 \pm 7\mu b, \sigma(D^o/\overline{D}^o) = 26^{+21}_{-13}\mu b).$$

We have also measured the longitudinal and transverse momentum distributions of observed D meson decays. The x_F distribution was well parametrized by

$$\frac{dN}{dx_F} \sim (1 - |x_F|)^n, n = 11.0^{+4.6}_{-3.6},$$

and the p_T distribution was well parametrized by

$$rac{dN}{dp_T^2} \sim exp(-bp_T^2), b = 0.66^{+0.23}_{-0.20} (GeV/c)^{-2}.$$

When compared with measurements made at lower energies, our results imply a slowly rising D meson cross section with center of mass energy,

$$rac{\sigma_{D\overline{D}}(\sqrt{s}=38GeV)}{\sigma_{D\overline{D}}(\sqrt{s}=27GeV)}=1.7^{+0.6}_{-0.5}.$$

Furthermore we observe no events at $|x_F| > 0.3$, which corresponds to an upper limit of 10 μ b at a 95% confidence level for D production at large x_F .

Also measured were the associated charged multiplicity in both charm and non-charm events. For charm events the mean primary multiplicity was $\langle N_{ch} \rangle = 11.9 \pm 1.0, pp \rightarrow \text{charm} + \text{X}$, while for inclusive proton-proton events $\langle N_{ch} \rangle = 10.26 \pm 0.15, \langle N_{ch,non-diffractive} \rangle = 11.59 \pm 0.16, (\geq 6 \text{ prongs}).$

The weak energy dependence of the total cross section and the predominantly central character of D meson production are in sharp contrast with results from a number of experiments at the CERN ISR which reported copious charm production in the forward region^{1,2}, $\sigma_{charm} \approx 1mb$, $\frac{d\sigma}{da_F} \sim$ flat.

We have shown that the flavor excitation model and the intrinsic charm model, invoked at the time of the reports from the ISR, are unnecessary to explain our results on the production dynamics and on the energy dependence of the cross section for D mesons. There is now a consensus that although the intrinsic charm model cannot be eliminated, contributions to charm production by that mechanism are likely to be small³.

¹S. L. Olsen, AIP Conference Proceedings No. 85 (1981) 1

²D. DiBitonto, AIP Conference Proceedings No. 85 (1981) 26

⁸J. L. Ritchie, Procs. of the 1984 Summer Study, Snowmass, Colorado (1984) 237

In conclusion, we have made a precise measurement of the hadronic charm production cross section at $\sqrt{s}=39$ GeV. When compared to measurements made at lower energies, our results indicate a relatively weak energy dependence for the charm cross section. Along with our observation of a predominantly central longitudinal production momentum distribution for charm, the observed energy dependence eliminated the flavor excitation model and the intrinsic charm model for charm production at $\sqrt{s} \leq 39$ GeV. The fact that the non-diffractive component of the mean inclusive multiplicity was approximately the same as that observed for charm associated events provides additional evidence that charm production is non-diffractive, in contrast with the above mentioned models. The more generally accepted fusion model, on the other hand, can reproduce most aspects of our data.

Appendix A

THE IMPACT PARAMETER OF DECAY TRACKS

The impact parameter of a decay track is defined as $Y = L \sin \theta$ where L is the decay length and θ is the angle of the decay track relative to the direction of its parent. We show here that, when the Q value of the decay is large and the Lorentz boost from the rest frame of the parent to the laboratory frame is also large, the impact parameter of decay tracks is independent of the parent momentum.

Let $q_{||}$ and q_{\perp} be the components of the daughter momenta along and normal to the parent line of flight in the laboratory frame,

$$q_{\perp}=q^{*}\sin heta^{*},$$

$$q_{||}=\gamma(q^*\cos heta^*+eta\sqrt{q^{*2}+m^2}),$$

where q^* is the daughter momentum is the parent rest frame and m is the daughter mass (the superscript * denotes the parent rest frame). The decay angle in the laboratory frame is

$$\sin heta = rac{q_{\perp}}{q} = rac{q^{st} \sin heta^{st}}{\sqrt{q^{st 2} \sin^2 heta^{st} + \gamma^2 (q^{st} \cos heta^{st} + eta \sqrt{q^{st 2} + m^2})^2}}.$$

In the limit of large Q values $(q^* \gg m)$,

$$\sin heta \simeq rac{\sin heta^*}{\sqrt{\gamma^2 (\cos heta^* + eta)^2 + \sin^2 heta^*}},$$

and in the limit of a large Lorentz boost from the parent rest frame to the laboratory $(\beta \simeq 1, \gamma \gg 1),$

$$\sin heta \simeq rac{\sin heta^*}{\gamma (1+\cos heta^*)} = rac{1}{\gamma} an rac{ heta^*}{2}.$$

The decay angle in the laboratory frame decreases as $\frac{1}{\gamma}$. The decay length is $L = \gamma \beta c \tau$ where τ is the proper decay time, so that the impact parameter is

$$Y \simeq c au an rac{ heta^*}{2},$$

independent of the parent momentum.

For an isotropic angular distribution of decay products in the parent rest frame $(\frac{dN}{d\Omega} = \text{constant})$, the above approximate expression for Y can be integrated and yields a mean impact parameter of $< Y > \simeq c\tau$.

Appendix B

SIMULATING CHARM DECAYS

We describe here an algorithm developed by the author to simulate charm decays in Monte Carlo calculations used throughout this thesis.

Since flavor is conserved in the strong interaction charm is hadronically produced in pairs. There has been no experimental indication of momentum or angular correlations between the pair produced charmed hadrons. Open charm, i.e. hadrons with nonzero charm quantum number, decays weakly. Due to the vastly different time scales involved, the production and decay of charm particles can be treated as independent processes.

Figure 1(a) shows the proper decay time distribution for simulated $D^+ \to K^-\pi^+\pi^+$ events, and Figure 1(b) shows the D meson transverse momentum distribution for these events. We have used the inclusive distributions

$$rac{d\sigma}{dx_F} \sim (1-|x_F|)^n, rac{d\sigma}{dv_T^2} \sim e^{-bp_T^2}, rac{d\sigma}{dt} \sim e^{-t/ au},$$

to simulate hadronic charm production. Also shown in Figures 1(c) and 1(d) are the laboratory momentum distribution for these D mesons and the decay length distribution.

Assuming that the matrix elements for charm decays are constants, decay momenta are governed solely by phase space probabilities. We have used a cascade decay model in our simulation of charm decays: a parent particle disintegrates into a series of two body systems which in turn decay into the daughters of the final state. The phase space probability dP_n/dp_n for the final state momentum configuration $(p_n, p_{n-1}, ..., p_1)$ was calculated according to the recursive formula

$$rac{dP_3}{dp_3} = rac{\pi^2 p_3^2}{e_3} rac{\sqrt{(s+m_3^2 - 2e_3\sqrt{s} - m_1^2 - m_2^2)^2 - 4m_1^2 m_2^2}}{s+m_3^2 - 2e_3\sqrt{s}}, \ rac{dP_n}{dp_n} = rac{2\pi p_n^2}{e_n} imes (rac{dP_{n-1}}{dp_{n-1}})$$

where n is the number of final state particles and \sqrt{s} is the available energy. Figure 2(a) shows the distribution of daughter momenta for simulated $D^+ \to K^-\pi^+\pi^+$ decays and Figure 2(b) shows the daughter transverse momentum distribution, in the rest frame of the parent particle. Figures 2(c) and 2(d) show the angular distributions $dN/d\phi$ and $dN/d(\cos\theta)$ of the decay products in the rest frame of the parent. When Lorentz boosted into the laboratory frame, these daughter momenta and angles give rise to the impact parameter distribution of Figure 1(e), and the distribution in Figure 1(f) of decay angles with respect to the line of flight of the parent.

Figure B.1: Simulated $D^- \to K^-\pi^-\pi^-$ decays, part 1:

 $(a)d\mathcal{N}/d(ct(mm)).\ (b)d\mathcal{N}/d(p_T^2((GeV/c)^2)),\ (c)d\mathcal{N}/d(p_{lab}(GeV/c))\ .$

 $(d)dN/dL(mm), (e)dN/d(sin\theta), (f)dN/dY(mm).$

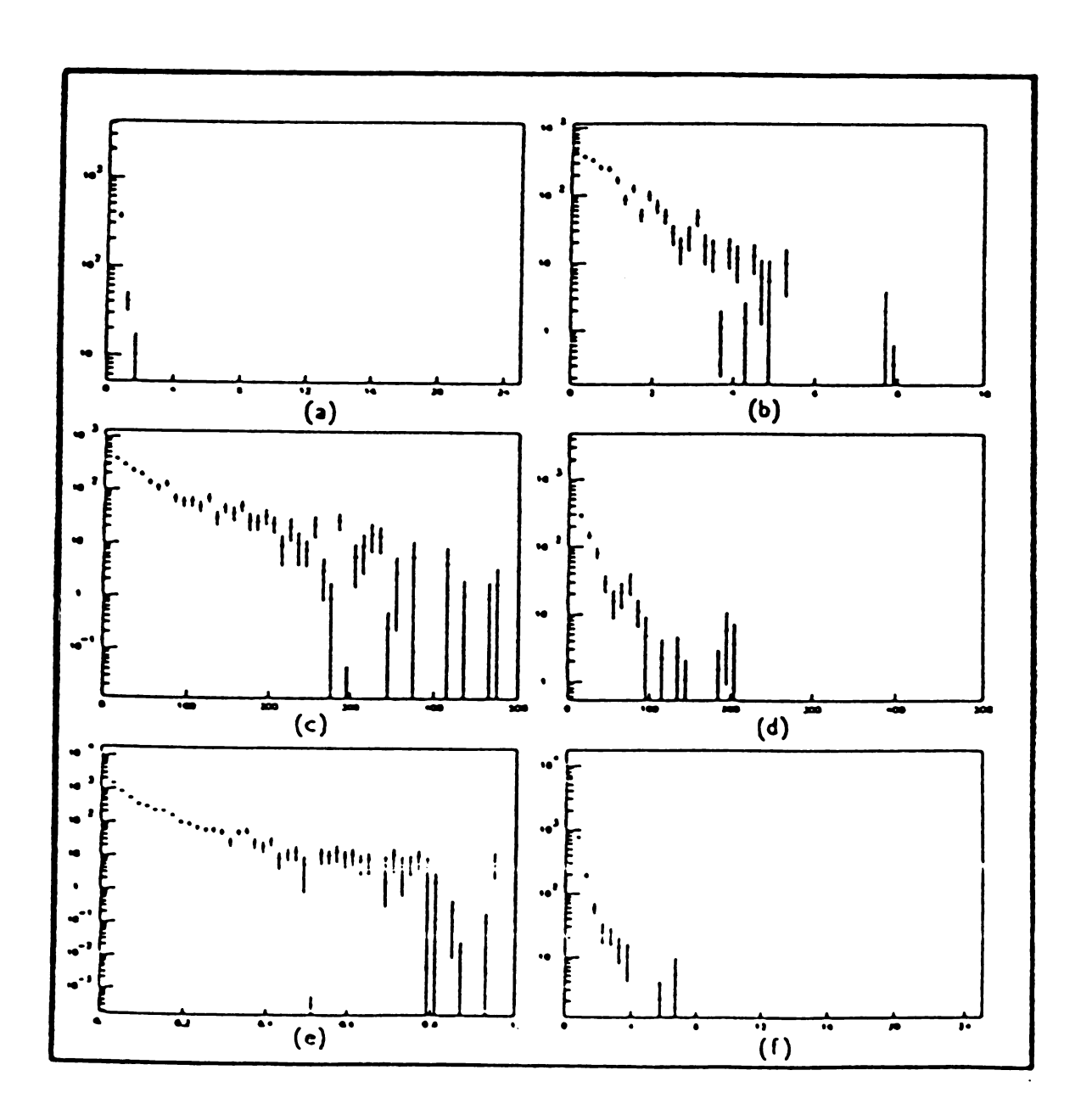
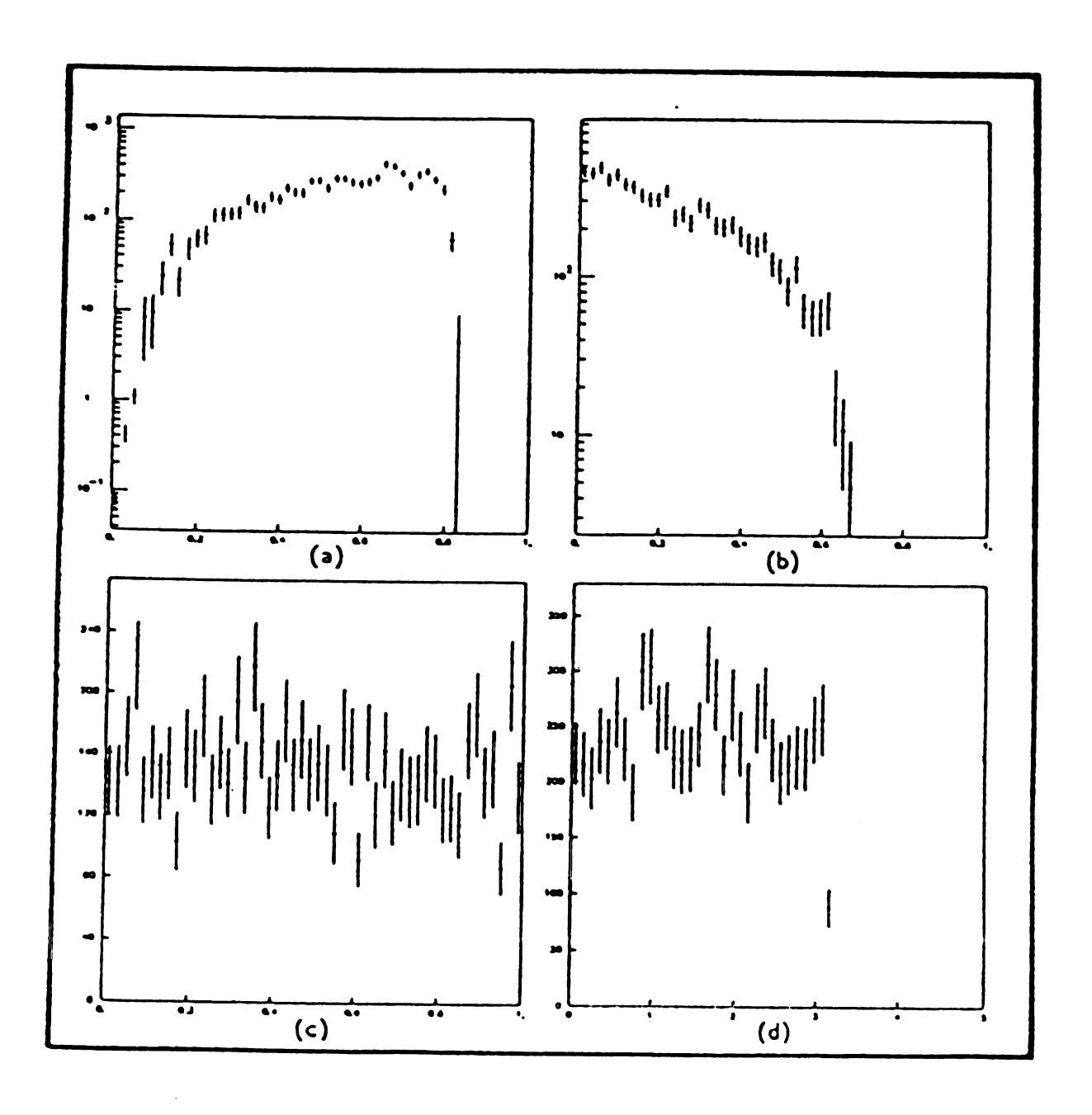


Figure B.2: Simulated $D^- \to K^-\pi^-\pi^-$ decays, part 2: (a)dN/dq(GeV/c), (b) $dN/d(q_T^2((GeV/c)^2))$, (c) $dN/d(cos\theta)$, (d) $dN/d\phi(radians)$.



Appendix C

THE 0°C CALCULATION

We describe here the 0°C calculation, a procedure developed to obtain kinematic solutions to charm decays¹.

Under the assumption that all of the decay products are charged, constrained kinematic fits were attempted in order to determine the momentum of the parent. When all charged decay products were reconstructed in the spectrometer but no constrained fits were found, indicating that one of the decay products was neutral, unconstrained (0C) calculations were used to obtain the momentum of the parent. In cases where no constrained fits were found and one charged decay product was outside the spectrometer acceptance, the 0°C calculation was used to obtain the parent momentum.

The 0*C calculation treats the case

$$D o (\Sigma_{rec} \pi) + X_{mis}$$

where the sum extends over all reconstructed charged tracks and X_{mis} denotes a

¹C. Bromberg and A. Nguyen, E743 internal note

system of particles with an invariant mass $m_{mis} = 500$ MeV. The parent momentum p_D was calculated using

$$p_D^2 - p_D rac{\mu^2 p_{rec,||}}{E_{rec}^2 - p_{rec,||}^2} + rac{4 E_{rec}^2 m_D^2 - \mu^4}{4 (E_{rec}^2 - p_{rec,||}^2)} = 0$$

where

$$\mu \equiv \sqrt{m_D^2 + m_{rec}^2 - m_{mis}^2}$$

The subscript || denotes the component of the momentum along the direction of flight of the parent.

In general there were two solutions to the above quadratic equation in p_D , a fast (high laboratory momentum) and a slow (low laboratory momentum) solution. Since these events have lost at least one low momentum decay track the phase space probability of the two solutions heavily favors the slow solution, i.e. if the parent had the high momentum of the fast solution all charged decay products would have been within the spectrometer acceptance and would have been reconstructed. Therefore only the slow solution was used.

Corrections for the slow solution were evaluated by Monte Carlo. D meson decays were generated and the slow 0°C solution was used to calculate x_F' for decays with one charged daughter outside the spectrometer acceptance. Table 1 shows $\langle x_F - x_F' \rangle$ where x_F is the actual Feynman x of the parent. As can be seen the corrections were small ($\langle 0.1 \rangle$) over the x_F range where charged decay tracks were lost outside the spectrometer.

In order to test the 0°C procedure, charm decays were generated with the al-

Table C.1: Corrections for the slow 0°C solution; R denotes a reconstructed charged track, L denotes a charged track lost outside the spectrometer acceptance, and O denotes one or more missing neutrals.

Topology	x_F'	$< x_F - x_F^\prime >$
$C3 \rightarrow RRLO$	-0.25	0.09 ± 0.04
	-0.15	0.05 ± 0.03
	-0.05	$\textbf{0.04} \pm \textbf{0.02}$
	0.05	0.04 ± 0.03
$V4 \rightarrow RRRLO$	-0.25	0.09 ± 0.04
	-0.15	$\textbf{0.04} \pm \textbf{0.02}$
	-0.05	0.02 ± 0.02
	0.05	0.02 ± 0.02

gorithm described in Appendix A. In decays with missing neutrals and one missing charged daughter the slow 0°C solution for the parent momentum was used to calculate x_F' ; the x_F' distribution was corrected using the results in Table 1. The corrected distribution reproduced well the generated distribution.

